

**1 Earthquake nucleation on rate and state faults –**  
**2 Aging and slip laws**

Jean-Paul Ampuero

**3** Institute of Geophysics, ETH Zurich, Switzerland

Allan M. Rubin

**4** Department of Geosciences, Princeton University, Princeton, New Jersey,

**5** USA

---

J.-P. Ampuero, Institute of Geophysics, Seismology and Geodynamics ETH Honggerberg  
(HPP) CH-8093 Zurich Switzerland (email: [ampuero@erdw.ethz.ch](mailto:ampuero@erdw.ethz.ch))

A. M. Rubin, Department of Geosciences, Princeton University, Princeton, NJ 08544, (email:  
[arubin@princeton.edu](mailto:arubin@princeton.edu))

**Abstract.** We compare 2-D, quasi-static earthquake nucleation on rate- and-state faults under both “aging” and “slip” versions of the state evolution law. For both versions mature nucleation zones exhibit 2 primary regimes of growth: Well above and slightly above steady state, corresponding respectively to larger and smaller fault weakening rates. Well above steady state, aging-law nucleation takes the form of accelerating slip on a patch of fixed length. This length is proportional to  $b^{-1}$  and independent of  $a$ , where  $a$  and  $b$  are the constitutive parameters relating changes in slip speed and state to frictional strength. Under the slip law the nucleation zone is smaller and continually shrinks as slip accelerates. The nucleation zone is guaranteed to remain well above steady state only for values of  $a/b$  that are low by laboratory standards. Near steady state, for both laws the nucleation zone expands. The propagating front remains well above steady state, giving rise to a simple expression for its effective fracture energy  $G_c$ . This fracture energy controls the propagation style. For the aging law  $G_c$  increases approximately as the square of the logarithm of the velocity jump. This causes the nucleation zone to undergo quasi-static crack-like expansion, to a size asymptotically proportional to  $b/(b - a)^2$ . For the slip law  $G_c$  increases only as the logarithm of the velocity jump, and crack-like expansion is not an option. Instead, the nucleation zone grows as an accelerating unidirectional slip pulse. Under both laws the nucleation front propagates at a velocity larger than the slip speed by roughly  $\mu'/b\sigma$  divided by the logarithm of the velocity jump, where  $\mu'$  is the effective elastic shear modulus. For this prediction to be con-

29 sistent with observed propagation speeds of slow slip events in subduction  
30 zones appears to require effective normal stresses as low as 1 MPa.

## 1. Rate-and-state background

31 Although the modern rate- and state-dependent friction equations have been in use for  
 32 over 20 years, their implications for earthquake nucleation on deformable faults remain  
 33 unclear. In their simplest and most common form, the frictional strength  $\tau$  is written as

$$34 \quad \tau = \sigma \left[ f^* + a \ln \frac{V}{V^*} + b \ln \frac{V^* \theta}{D_c} \right], \quad (1)$$

35 where  $\sigma$  is the effective normal stress, here assumed constant, and  $f^*$  and  $V^*$  are reference  
 36 values of the friction coefficient and sliding velocity. The rate-dependent part of the  
 37 strength, proportional to the logarithm of the sliding velocity  $V$  and the constitutive  
 38 parameter  $a$ , is thought to reflect a thermally-activated Arrhenius process involving the  
 39 breaking of atomic bonds at contact points bridging the sliding surface [Rice *et al.*, 2001].  
 40 The state-dependent part of the strength, proportional to the logarithm of the state  
 41 variable  $\theta$  and the parameter  $b$ , is more mysterious, “state” being more difficult to observe  
 42 than sliding velocity, but  $\theta$  is thought to reflect the product of the true contact area and  
 43 the intrinsic strength of those contacts.

44 Two empirical equations for the evolution of  $\theta$ , first formalized by *Ruina* [1983], are in  
 45 common use. These are

$$46 \quad \dot{\theta} = 1 - \frac{V\theta}{D_c} \quad (\text{Aging law}) ; \quad (2)$$

$$47 \quad \dot{\theta} = -\frac{V\theta}{D_c} \ln \frac{V\theta}{D_c} \quad (\text{Slip law}) ; \quad (3)$$

49 where  $D_c$  is a characteristic slip distance. We refer to the first as the “aging law” because  
 50 at zero slip speed  $\theta$  increases as elapsed time. Under the second law  $\dot{\theta} = 0$  when  $V = 0$ ;

51 that is,  $\theta$  evolves with slip alone. Both laws exhibit steady-state behavior ( $\dot{\theta} = 0$ ) when  
 52  $V\theta/D_c = 1$ . If one interprets  $D_c$  as a typical contact size [*Dieterich and Kilgore, 1994*],  
 53 then at steady state  $\theta$  represents a typical contact lifetime  $D_c/V$ . Because of this, and  
 54 because of the behavior at  $V = 0$  for the aging law,  $\theta$  is sometimes thought of as contact  
 55 age [e.g., *Dieterich and Kilgore, 1996*]. However, even for the aging law this simple  
 56 interpretation breaks down if  $V\theta/D_c$  differs from 0 or 1.

57 In the vicinity of steady state,  $\ln(V\theta/D_c) \approx V\theta/D_c - 1$  and the two laws are asymp-  
 58 totically identical. Far from steady state this similarity disappears. Figure 1 shows the  
 59 stress evolution during hypothetical velocity-stepping experiments, of the sort that ex-  
 60 perimentalists conduct but with much larger velocity jumps, for both laws. The surface  
 61 was sliding with velocity  $V_1$  and state  $\theta_1$  prior to the jump, and the subsequent velocity  
 62  $V_2$  is chosen to produce ratios  $\theta_1/\theta_2$  of  $\pm 1 - 4$  orders of magnitude, where  $\theta_2 \equiv D_c/V_2$  is  
 63 the future steady-state value (these are equivalent to velocity jumps of  $\pm 1 - 4$  orders of  
 64 magnitude if at the time of the jump the surface had been sliding at steady state). For  
 65 constant  $V_2$  equations (2) and (3) can be integrated to yield

$$66 \quad \theta = \theta_2 + (\theta_1 - \theta_2)e^{-\delta/D_c} \quad (\text{Aging law}) ; \quad (4)$$

$$67 \quad \theta = \theta_2(\theta_1/\theta_2)^{\exp(-\delta/D_c)} \quad (\text{Slip law}) ; \quad (5)$$

69 where  $\delta$  is slip since the velocity jump. Substituting into (1), relative to the future steady-  
 70 state value  $\tau_2$  the stress is

$$71 \quad \tau - \tau_2 = b\sigma \ln \left[ 1 + \frac{(\theta_1 - \theta_2)e^{-\delta/D_c}}{\theta_2} \right] \quad (\text{Aging law}) ; \quad (6)$$

$$72 \quad \tau - \tau_2 = b\sigma \ln(\theta_1/\theta_2)e^{-\delta/D_c} \quad (\text{Slip law}) . \quad (7)$$

74 Independent of the evolution law, the stress immediately following the velocity jump  
 75 exceeds the future steady-state value by  $b\sigma \ln(\theta_1/\theta_2)$  (independent because the steady  
 76 state values are the same and as of yet there has been no evolution).

77 For the aging law the following approximations accurately describe the stress evolution  
 78 following large velocity increases and decreases, respectively:

$$79 \quad \tau - \tau_2 \approx b\sigma [\ln(\theta_1/\theta_2) - \delta/D_c] , \quad \theta \gg \theta_2 ; \quad (8)$$

$$80 \quad \tau - \tau_2 \approx b\sigma \ln [1 - e^{-\delta/D_c}] , \quad \theta \gg \theta_1 . \quad (9)$$

82 The asymmetric response (Figure 1a) derives from the relative importance of time-  
 83 dependent healing. For large velocity increases  $V_2\theta_1/D_c \gg 1$ , the constant term in (2)  
 84 is initially negligible,  $\theta$  evolves with slip but not time, and  $\tau$  decreases linearly with slip  
 85 according to (8). For large velocity decreases  $V_2\theta_1/D_c \ll 1$ , so  $\theta$  initially evolves linearly  
 86 with time and substantial evolution occurs over slip distances  $\delta/D_c \ll 1$ .

87 It has long been recognized that velocity-stepping experiments exhibit rather symmetric  
 88 behavior in response to velocity increases and decreases, consistent with the slip law  
 89 [e.g., *Blanpied et al.*, 1998]. But in other ways this law is deficient. Using a servo-  
 90 control system to alter the effective stiffness of their testing apparatus, *Beeler et al.*  
 91 [1994] found evidence that the frictional surface heals with time, rather than with ever-  
 92 decreasing slip rate, during “slide-hold-slide” experiments. In addition, *Dieterich and*  
 93 *Kilgore* [1994] observed microscopically that the true contact area increases with time  
 94 during the stationary contact of two surfaces, presumably as a result of time-dependent  
 95 deformation of asperities. Because the slip law is unable to account for this observed time-  
 96 dependence, it appears that the aging law has become the law of choice among modelers

97 over the last decade. It is also the case that most velocity-stepping experiments have  
 98 been restricted to jumps of a single order of magnitude, where the asymmetric response  
 99 of the aging law is somewhat subdued. However, our simulations suggest that it is the  
 100 response of the fault surface near to and well above steady state that most strongly  
 101 influences nucleation, and not the response well below steady state where the slip law  
 102 appears to be inadequate. The response well above steady state is important because  
 103 growing nucleation zones impose large and abrupt velocity increases in areas that were  
 104 previously nearly locked, e.g. as a result of a prior earthquake. As we will show, the  
 105 effective fracture energy of such a nucleation front is well-approximated by the area under  
 106 the appropriate curve in Figure 1. This fracture energy in turn controls the nucleation  
 107 style, which may differ markedly for the two evolution laws (Figure 2).

108 Equations (1)–(3) have received considerable attention in the context of spring-block  
 109 sliders ( $\dot{\tau} = k[V^* - V]$ , where  $k$  is the spring stiffness,  $V^*$  is the load-point velocity, and  
 110 dots denote time derivatives). For the aging law, a necessary but not sufficient condition  
 111 for instability, in the sense that neglect of inertia leads to infinite slip speeds, is that  
 112  $a < b$ ; that is, that the surface be steady-state velocity weakening. *Ranjith and Rice*  
 113 [1999] showed that for arbitrary perturbations from steady state, instability also requires  
 114 that the spring stiffness be less than a critical value given by

$$k_{cr} = \frac{\sigma(b - a)}{D_c} . \quad (10)$$

116 Because the two laws are asymptotically identical near steady state, for infinitesimal per-  
 117 turbations from steady sliding the same  $k_{cr}$  applies to the slip law. However, nonlinear  
 118 stability analysis for the slip law indicates that for sufficiently large perturbations instabil-

ity is possible for  $k > k_{cr}$  [Gu *et al.*, 1984]. This property of the slip law has implications for nucleation on deformable faults, even under slow background loading, because the evolving nucleation zone provides its own large perturbation.

The concept of a unique critical stiffness does not have a simple extension to deformable faults. Nonetheless, the following dimensional estimate is instructive. The effective stiffness at the center of a 2-D elastic crack (the stress drop for a given slip) is  $k^* \equiv \Delta\tau/\delta = \mu'/2L$ , where  $2L$  is the crack length and  $\mu'$  is the shear modulus  $\mu$  for anti-plane strain and  $\mu/(1-\nu)$ , where  $\nu$  is Poisson's ration, for plane strain. Setting this  $k^*$  equal to  $k_{cr}$  for a spring-block slider leads to the following estimate for the minimum half-length of a nucleation zone capable of instability:

$$L_{min} \sim \frac{1}{2} \frac{\mu' D_c}{(b-a)\sigma} . \quad (11)$$

To within a constant coefficient this is the critical size  $h^*$  introduced by Rice [1993]. Somewhat surprisingly, in a numerical study of the aging law Dieterich [1992] found that nucleation zones localized to a fixed length that scaled as  $b^{-1}$ , rather than  $(b-a)^{-1}$ , when  $V\theta/D_c$  was much greater than 1. For  $V\theta/D_c$  closer to steady state, on the other hand, the nucleation zone expanded during the approach to instability. Because the following terms occur repeatedly in this paper, we define

$$L_b \equiv \frac{\mu' D_c}{b\sigma} ; \quad (12)$$

$$\Omega \equiv \frac{V\theta}{D_c} . \quad (13)$$

139 For  $\Omega > 1$  the fault is above steady state and would weaken at constant slip speed, whereas  
140 for  $\Omega < 1$  the fault is below steady state and would strengthen at constant slip speed.  
141 Throughout this paper we use “steady state” to mean  $\Omega = 1$ , without implying anything  
142 about the slip speed relative to the driving or plate rate.

143 *Rubin and Ampuero* [2005a] obtained analytical estimates for the nucleation length and  
144 time-to-failure for deformable faults obeying the aging law. They identified two regimes,  
145 distinguished by the behavior of  $\Omega$ : Well above steady state ( $\Omega \gg 1$ ) everywhere, the  
146 regime emphasized by *Dieterich* [1992], and well above steady state only at the margins  
147 of the nucleation zone, with sliding being slightly above steady state ( $\Omega \gtrsim 1$ ) in the  
148 interior. Well above steady state, nucleation localizes to a fixed length close to  $L_b$ , as  
149 found by *Dieterich*. A separable solution for this regime shows that only for  $a/b < 0.3781$   
150 does  $\Omega$  increase during the approach to instability. For larger values,  $\Omega$  is eventually driven  
151 down to an  $a/b$ -dependent value near 1. In this regime nucleation zones expand quasi-  
152 statically and asymptotically approach a value proportional to  $[b/(b - a)]^2 L_b$ , although  
153 how closely they approach this value before reaching dynamic slip speeds depends upon  
154 the loading conditions.

155 Laboratory values of  $a/b$  are typically larger than 0.5, and a reasonable median value  
156 appears to be 0.9 even on velocity-weakening surfaces [*Kilgore et al.*, 1993; *Blanpied et al.*,  
157 1998, using  $a/(b_1 + b_2)$  for the 2-state-variable fits of the latter]. Near the base of the  
158 seismogenic zone, where loading rates are high and many large earthquakes seem to nu-  
159 cleate,  $a/b$  is expected to be close to 1 if, as is believed, this region marks the transition  
160 from velocity-weakening to velocity-strengthening behavior. The nucleation length for  
161  $a/b = 0.95$  can exceed that of the fixed-length solution by a factor of 100. For lab values

162 of  $a$  and  $b$  ( $\sim 0.01$ ) and  $D_c$  near the upper end of laboratory measurements ( $\sim 100\mu\text{m}$   
 163 [*Marone, 1998*]), such a nucleation zone could be more than 1 km across, raising the pos-  
 164 sibility that it could be detected remotely. However, this large size is directly traceable  
 165 to the large area beneath the aging law stress-displacement curves in Figure 1a. As was  
 166 noted by *Nakatani* [2001], this prediction of the aging law is contradicted by laboratory  
 167 experiments. Therefore in this paper we explore the slip law, which we find exhibits  
 168 the same two general nucleation regimes, if not the same behavior. We begin by briefly  
 169 reviewing and slightly extending the aging law results of Rubin and Ampuero, because  
 170 these are useful for interpreting the slip law simulations. The latter have proven to be  
 171 more resistant to simple analytical approximations.

## 2. Numerical method

172 In the quasi-static limit we equate the frictional strength with the fault stress, which is  
 173 partitioned into a boundary condition  $\tau^\infty$  and an elastic component  $\tau^{el}$  due to nonuniform  
 174 slip. In two dimensions the static elastic stresses are proportional to the Hilbert transform  
 175  $\mathcal{H}$  of the along-fault slip gradient  $\delta'$ :

$$176 \quad \tau(x) = \tau^\infty(x) + \tau^{el}(x) = \tau^\infty(x) + \frac{\mu'}{2}\mathcal{H}[\delta'](x). \quad (14)$$

177 Equating (1) and (14) and differentiating with respect to time yields

$$178 \quad a\frac{\dot{V}}{V} + b\frac{\dot{\theta}}{\theta} = \frac{\dot{\tau}^\infty}{\sigma} + \frac{\mu'}{2\sigma}\mathcal{H}[V']. \quad (15)$$

179 The parameters  $\sigma$ ,  $a$ ,  $b$ , and  $\dot{\tau}^\infty$  are taken to be constant and uniform. Equations (15)  
 180 and (2) or (3) are solved using the numerical scheme of *Rubin and Ampuero* [2005a]. For

181 growing nucleation zones the propagating front remains well above steady state, with the  
 182 result that the smallest length scale to be resolved numerically scales roughly as  $L_b$  for  
 183 the aging law and  $L_b$  divided by the logarithm of the velocity jump for the slip law. For  
 184 the slip law at near-dynamic speeds this is much smaller than the critical cell size  $h^* \sim$   
 185  $\mu' D_c / \sigma(b-a)$  introduced by *Rice* [1993] (by a factor of  $\sim 100$  for  $a/b = 0.75$ ). We settled on  
 186 grid spacings of  $L_b/50 - L_b/150$ , which for the aging law is finer than necessary. Simulations  
 187 were carried out in double precision because for the slip law single precision sometimes  
 188 gave rise to asymmetric nucleation from symmetric initial and boundary conditions. We  
 189 use  $D_c = 400 \mu\text{m}$ ,  $\mu' = 11.56 \text{ GPa}$ ,  $\sigma = 100 \text{ MPa}$ , and  $b = 0.01$ . As we present results  
 190 with lengths normalized by  $L_b$  and slips by  $D_c$  these choices are largely irrelevant (they  
 191 influence the simulations only through the scaling of the initial or boundary conditions).

### 3. Aging law nucleation

#### 3.1. Well above steady state

192 For low values of  $a/b$ , the nucleation zone accelerates at fixed length while maintaining  
 193  $\Omega \gg 1$  (e.g., Figure 1 of *Rubin and Ampuero* [2005a]). The latter observation motivates  
 194 approximating the aging law (2) as

$$\dot{\theta} = -\Omega \tag{16}$$

196 [*Dieterich*, 1992]. The similar appearance of successive velocity profiles suggests a separable  
197 rable solution of the form

$$198 \quad V(x, t) = V_o(t)\mathcal{V}(x/L), \quad |x| < L; \quad (17)$$

$$199 \quad V(x, t) = 0, \quad |x| \geq L,$$

$$200 \quad \dot{\tau}^{el}(x, t) = V_o(t) \frac{\mu'}{2L} \dot{\mathcal{T}}(x/L), \quad (18)$$

202 where  $L$  is the fixed effective crack length, the velocity distribution  $\mathcal{V}$  is a function of  
203 dimensionless position  $x/L$ , normalized such that  $\mathcal{V}(0) \equiv 1$ , and  $\dot{\mathcal{T}}$  is the elastic stressing  
204 rate. Substituting (16)–(18) into (15), *Rubin and Ampuero* [2005a] obtained a solution  
205 with the following properties:

206 (1) For slip speeds large enough that the remote loading rate is negligible ( $\dot{\tau}^{el} \gg \dot{\tau}^\infty$ ),

207  $V_o$  evolves according to

$$208 \quad \frac{\dot{V}_o}{V_o^2} = \frac{b}{a} \left[ 1 + \frac{L_b}{2L} \dot{\mathcal{T}}(0) \right] \frac{1}{D_c} \equiv \frac{C_{\Omega \gg 1}}{D_c}, \quad (19)$$

209 with solution

$$210 \quad V_o(t) = \frac{D_c}{C_{\Omega \gg 1}} (t^* - t)^{-1} ; \quad t^* \equiv D_c / C_{\Omega \gg 1} V_o(0) . \quad (20)$$

211 For  $C_{\Omega \gg 1} > 0$ , infinite velocities are reached at a finite time  $t^*$ .

212 (2)  $\mathcal{V}$  and  $\dot{\mathcal{T}}$  are determined by using elasticity to solve

$$213 \quad \mathcal{V} = 1 - \frac{L_b}{2L} \left[ \dot{\mathcal{T}}(\xi) - \dot{\mathcal{T}}(0) \right] , \quad \left| \xi \equiv \frac{x}{L} \right| \leq 1 , \quad (21)$$

214 an eigenvalue problem that has solutions for all values of the dimensionless nucleation  
215 length  $L/L_b$ . Adding the constraint that the stresses outside the nucleation zone remain

216 finite, expressed as a stress intensity factor equal to zero, fixes  $L$  and  $C_{\Omega \gg 1}$  to the unique  
 217 values

$$218 \quad L_\nu \approx 1.3774L_b ; \quad (22)$$

$$219 \quad C_{\Omega \gg 1} \approx 0.3781 \frac{b}{a}. \quad (23)$$

221 (3) For  $\dot{\tau}^{el} \gg \dot{\tau}^\infty$ , the evolution of  $\Omega$  is given by

$$222 \quad \frac{\Omega(\xi, t)}{\Omega(\xi, 0)} = \left( \frac{V_o(t)}{V_o(0)} \right)^{1 - \mathcal{V}(\xi)/C_{\Omega \gg 1}}. \quad (24)$$

223 Equation (24) shows that  $\Omega$  decreases with increasing slip speed for  $\mathcal{V}(\xi)/C_{\Omega \gg 1} > 1$ .  
 224 Because  $\mathcal{V}$  is maximal at the crack center,  $\Omega$  decreases most rapidly (if at all) at  $x/L = 0$ .  
 225 Substituting  $\mathcal{V}(0) = 1$  and (23) into (24), the nucleation zone remains well above steady  
 226 state until instability only for

$$227 \quad \frac{a}{b} < \sim 0.3781. \quad (25)$$

228 It is instructive to compare (24) to the corresponding expression for a spring-block slider  
 229 with stiffness  $k$ . Substituting into (15)  $\dot{\theta} = -V\theta/D_c$  and  $\dot{\tau} = -kV$  (the latter assuming  
 230 negligible load-point velocity) leads to  $C_{\Omega \gg 1} = (b/a)[1 - kD_c/b\sigma]$ . Equation (24) then  
 231 becomes

$$232 \quad \frac{\Omega(t)}{\Omega(0)} = \left( \frac{V(t)}{V(0)} \right)^{1 - \left[ \frac{a\sigma}{b\sigma - kD_c} \right]}. \quad (26)$$

233 Examination of the exponent in (26) shows that the classical requirement for instability  
 234 of a spring-block slider,  $k \leq k_{cr} = (b - a)\sigma/D_c$ , is identical to the requirement that  $\Omega$   
 235 not decrease with increasing slip speed. For a deformable fault that is well above steady  
 236 state, the interaction of the friction law with elasticity gives rise to an  $a/b$ -independent

237 nucleation length with a maximum stiffness that is less than  $k_{cr}$  for  $a/b < 0.3781$ , and more  
 238 than  $k_{cr}$  for  $a/b > 0.3781$ . This stiffness, reached at the crack center, is  $0.6219(b\sigma/D_c)$ .

### 3.2. Near steady state

239 We view the gross behavior of the nucleation zone as a competition between elasticity,  
 240 which tends to smooth velocity variations and hence promote expansion, and the effective  
 241 slip-weakening of the friction law, which favors localization. For  $\Omega \gg 1$  these two tenden-  
 242 cies apparently remain in balance and the nucleation zone accelerates at fixed length. For  
 243  $a/b > 0.3781$ ,  $\Omega$  increases as the fault passes through steady state from below, but then  
 244 decreases as the nucleation zone begins to localize (because its effective stiffness is too  
 245 large). As  $\Omega$  approaches steady state, the slip-weakening rate in the interior of the nucle-  
 246 ation zone decreases, tipping the prior balance in favor of elasticity, and the nucleation  
 247 zone expands in a crack-like fashion.

248 Figure 3 shows an example for  $a/b = 0.8$ . For a quasi-uniform stress drop  $\Delta\tau$  within  
 249 the interior of the nucleation zone (Figure 3d), the mechanical energy release rate  $G$  is

$$250 \quad G = \frac{\pi L}{2 \mu'} \Delta\tau^2 . \quad (27)$$

251 [*Lawn*, 1993]. The velocity jump experienced by material at the edge of the nucleation  
 252 zone is sufficiently abrupt that the effective fracture energy  $G_c$  is essentially the area  
 253 under the stress-vs.-displacement curves in Figure 1a. From equation (8), well above  
 254 steady state the slip weakening rate is constant,  $b\sigma/D_c$ , so the effective slip-weakening  
 255 distance  $\delta_c$  increases linearly with the near-tip peak-to-residual stress drop  $\Delta\tau_{p-r}$ . This

256 leads to

$$257 \quad G_c = \frac{\Delta\tau_{p-r}\delta_c}{2} = \frac{D_c}{2b\sigma}\Delta\tau_{p-r}^2. \quad (28)$$

258 Setting  $G = G_c$  and solving for the instantaneous nucleation length  $L$ ,

$$259 \quad L = \frac{L_b}{\pi} \left( \frac{\Delta\tau_{p-r}}{\Delta\tau} \right)^2. \quad (29)$$

260 Accounting for the quasi-constant value of  $\Omega$  in the nucleation zone (Figure 3c) leads

261 to

$$262 \quad \Delta\tau = \sigma[(b-a)\ln(V/V_{bg}) - b\ln(\Omega)]; \quad (30)$$

$$263 \quad \Delta\tau_{p-r} = b\sigma[\ln(V\theta_i/D_c) - \ln\Omega]; \quad (31)$$

265 where  $V_{bg}$  is defined as the hypothetical background velocity which at steady state would

266 give rise to the ambient stress  $\tau^\infty$ , and  $\theta_i$  is the (relatively unperturbed) value of state

267 ahead of the propagating nucleation front (Figure 3b). In the limit of large slip speeds the

268  $\ln(\Omega)$  terms in (30) and (31) may be neglected, and  $\ln(V\theta_i/D_c) \approx \ln(V/V_{bg})$ . Thus the

269 ratio  $\Delta\tau_{p-r}/\Delta\tau$  approaches  $b/(b-a)$ , and the nucleation length is predicted to approach

270 a limiting value  $L_\infty$  given by

$$271 \quad L_\infty = \frac{L_b}{\pi} \left( \frac{b}{b-a} \right)^2. \quad (32)$$

272 A constant  $\Omega$  implies  $\dot{V}/V + \dot{\theta}/\theta = 0$ . With  $\dot{\theta} = 1 - \Omega$  this leads to

$$273 \quad \frac{\dot{V}}{V^2} = \frac{1 - \Omega^{-1}}{D_c} \equiv \frac{C_{\Omega \sim 1}}{D_c}. \quad (33)$$

274 Thus equation (20) from Section 3.1 describes  $V(t)$ , but with a new definition of the

275 constant. Substituting  $-\dot{V}/V$  for  $\dot{\theta}/\theta$  in (15), writing  $-Vk^*$  for  $\dot{\tau}$  and rearranging leads

276 to

$$277 \quad \frac{\dot{V}}{V^2} = \frac{k^*}{\sigma(b-a)} ; \quad (34)$$

278 equating this with (33) shows that the stiffness needed to maintain the given  $\Omega$  is

$$279 \quad k^* = \frac{\sigma(b-a)}{D_c}(1 - \Omega^{-1}). \quad (35)$$

280 Note that this is smaller by the factor  $(1 - \Omega^{-1})$  than the critical stiffness for instability  
 281 given in (10), but equals the critical stiffness for a spring-block slider with zero load-point  
 282 velocity, as can be derived directly from equation (33) of *Ranjith and Rice* [1999].

283 *Rubin and Ampuero* [2005a] neglected expansion of the nucleation zone and equated  
 284  $k^*$  with  $\mu'/2L_\infty$ , appropriate for a crack of fixed length  $L_\infty$ . More properly, with  $\delta =$   
 285  $2L\Delta\tau/\mu'$ ,  $V = (2/\mu')(L\dot{\Delta}\tau + \dot{L}\Delta\tau)$ , so

$$286 \quad k^* = \frac{\dot{\Delta}\tau}{V} = \frac{\mu'}{2L_\infty} \left[ \frac{L}{L_\infty} + \frac{\Delta\tau}{\dot{\Delta}\tau} \frac{\dot{L}}{L_\infty} \right]^{-1}. \quad (36)$$

287 We find that with  $G_c$  proportional to  $\Delta\tau_{p-r}^2$ , changes in  $\Delta\tau$  and  $L$  are coupled such that  
 288 the increased stiffness that comes from a smaller nucleation zone is offset, analytically to  
 289 first order, by the decrease that comes from expansion (Appendix A). Thus the bracketed  
 290 expression remains close to unity, and  $k^*$  varies by much less than  $L/L_\infty$ . This helps  
 291 explain Rubin and Ampuero's observation that time-dependent simulations begin tracking  
 292 the predicted  $\Omega$  quite closely well before  $L$  reaches  $L_\infty$  (Figure 4), and, as this is only a  
 293 first-order result, their observation that the feedback maintaining the stiffness given by  
 294 (35) is imperfect.

295 Equating (35) with  $\mu'/2L_\infty$  (now with greater justification) and combining with (32)  
 296 leads to

$$297 \quad C_{\Omega \sim 1} \equiv 1 - \Omega^{-1} \approx \frac{\pi b - a}{2b} . \quad (37)$$

298 From (20), the time remaining to instability ( $t^* - t$ ) is  $C^{-1}D_c/V(t)$ , or

$$299 \quad t^* - t = \frac{2}{\pi} \frac{b}{b - a} \frac{D_c}{V(t)} . \quad (38)$$

300 Well above steady state, on the other hand, the comparable expression for the fixed-length  
 301 solution is (from (20) and (23))

$$302 \quad t^* - t = 2.645 \frac{a}{b} \frac{D_c}{V(t)} . \quad (39)$$

303 Except for  $a/b$  very near to either 0 or 1, the time remaining to instability is of the order  
 304 of  $D_c/V$  in both nucleation regimes.

305 Equation (32) for  $L_\infty$  provides an excellent fit to the largest nucleation lengths in the  
 306 simulations of *Rubin and Ampuero* [2005a] (their Figure 8a). For some boundary and  
 307 initial conditions, on the other hand, the nucleation zone was smaller and still expanding  
 308 when elastodynamic speeds were reached. A few examples are shown in Figure 4 for  $a/b =$   
 309 0.8. The solid curve, which asymptotes to the predicted  $L_\infty$  before a little complexity  
 310 sets in, is for a locally peaked initial load on an otherwise uniform surface. The dashed  
 311 curve is for the simulation of Figure 3, and the dotted curve is for the identical conditions  
 312 but with the initial values of  $\theta$  reduced by 4 orders of magnitude. In general, as in Figure  
 313 4, we find that the minimum value of  $L$  reached during a simulation decreases as the  
 314 maximum value of  $\Omega$  reached during the onset of nucleation increases, although never to

315 a value smaller than  $L_\nu$ , and that  $L$  at a given slip speed decreases as this  $\Omega_{max}$  increases  
 316 because this delays the approach to the  $\Omega \gtrsim 1$  solution.

## 4. Slip law nucleation

### 4.1. Well above steady state

317 For  $\Omega \gg 1$ , so that the aging law becomes  $\dot{\theta} \approx -\Omega$ , the two evolution laws differ by  
 318 the factor  $\ln(\Omega)$ . When substituted into (15), the resulting equations differ only in that  
 319  $b \ln(\Omega)$  in the slip law replaces  $b$  in the aging law:

$$320 \quad a \frac{\dot{V}}{V} - b \ln(\Omega) \frac{V}{D_c} = \frac{\dot{\tau}}{\sigma} \quad (\text{Slip law}) ; \quad (40)$$

$$321 \quad a \frac{\dot{V}}{V} - b \frac{V}{D_c} = \frac{\dot{\tau}}{\sigma} \quad (\text{Aging law, } \Omega \gg 1) . \quad (41)$$

323 Because of the logarithm, the factor  $\ln(\Omega)$  in (40) may be regarded as a slowly-varying  
 324 correction to  $b$  in (41). Since  $L_\nu$  for the aging law is inversely proportional to  $b$ , for the slip  
 325 law the nucleation zone can be expected to be smaller by roughly  $\ln(\Omega)$ . Well above steady  
 326 state, then, the nucleation zone slowly shrinks. This is shown in Figure 5a for  $a/b = 0.5$ .  
 327 The dashed lines show  $L_\nu$ , and the bold dotted lines  $L_\nu/\ln(\Omega)$ , with  $\Omega$  evaluated at the  
 328 center of the nucleation zone. The agreement with the numerical simulations is reasonably  
 329 good, but because of the non-constant  $\ln(\Omega)$  this scaling is not exact.

330 The acceleration of slip is also somewhat different under the two laws. For the aging law  
 331 in this regime  $\dot{V}/V^2 = C_{\Omega \gg 1}/D_c$ , where the constant  $C_{\Omega \gg 1}$  is given by equation (23). For  
 332 the slip law it is  $\dot{V}/(V^2 \ln \Omega)$  that remains approximately constant (Figure 6), as might  
 333 have been anticipated by substituting  $b \ln \Omega$  for  $b$  in (19). By analogy with the aging law,

334 we can define the (approximately) constant

$$335 \quad C' = D_c \frac{\dot{V}}{V^2 \ln \Omega} . \quad (42)$$

336 From the identity  $\dot{\Omega}/\Omega = \dot{\theta}/\theta + \dot{V}/V$  and the definition of the slip law,

$$337 \quad \frac{\dot{\Omega}}{\Omega} = \frac{\dot{V}}{V} - \frac{V}{D_c} \ln \Omega . \quad (43)$$

338 Combining (42) and (43) and integrating leads to

$$339 \quad \frac{\Omega}{\Omega_0} = \left( \frac{V}{V_0} \right)^{1-1/C'} , \quad (44)$$

340 where  $\Omega_0$  and  $V_0$  are initial values. This is analogous to equation (24) for the aging law,  
 341 so we expect the regimes  $\Omega \gg 1$  and  $\Omega \gtrsim 1$  to again be separated by  $C' = 1$ . We find  
 342 empirically that  $C'$  for the slip law exceeds  $C_{\Omega \gg 1}$  for the aging law at a given  $a/b$  (Figure  
 343 6b), implying that the transition to the  $\Omega \gtrsim 1$  regime occurs at larger  $a/b$  for the slip  
 344 law, and also that  $C'$  approaches 1 more gradually than  $C_{\Omega \gg 1}$ . Together with the fact  
 345 that  $C'$  is slightly variable during any given simulation (Figure 6), this means that the  
 346 transition to the  $\Omega \gtrsim 1$  regime for the slip law occurs over a modest range of  $a/b$ . For  
 347 the initial and boundary conditions of Figure 5 the transition begins between  $a/b = 0.5$   
 348 and 0.6 (Figure 5c), whereas for 2 different manifestations of a locally peaked stress on  
 349 an otherwise uniform surface it occurs for  $a/b$  between 0.6 and 0.7 (Figure 6b).

## 4.2. Near steady state

350 As with the aging law, for sufficiently large  $a/b$  the stiffness of the developing nucleation  
 351 zone is large enough that the interior is either driven down toward or never gets far above

352 steady state, and elasticity causes the nucleation zone to expand. And, as with the  
 353 aging law, the fault undergoes a sudden velocity increase as the edge of the nucleation  
 354 zone sweeps by, with the result that the effective fracture energy is given to a good  
 355 approximation by the area under the slip-vs.-displacement curves in Figure 1b. Integrating  
 356 equation (7) to infinite slip distances yields

$$357 \quad G_c = b\sigma \int_0^\infty \ln\left(\frac{V\theta_i}{D_c}\right) e^{-\delta/D_c} d\delta = b\sigma D_c \ln\left(\frac{V\theta_i}{D_c}\right) ; \quad (45)$$

358 integrating to only  $3D_c$  recovers 95% of this value. That the fracture energy increases  
 359 only as  $\ln(V)$  while the energy release rate grows as  $(\ln V)^2$  (equations 27 and 30) means  
 360 that, unlike the aging law, crack-like expansion is not an option. That is, in the limit of  
 361 large slip speeds the energy balance  $G = G_c$  for a hypothetical equilibrium crack becomes  
 362  $L(\ln V) = \text{constant}$ , indicating that acceleration of slip is incompatible with growth of the  
 363 nucleation zone.

364 We find instead that nucleation takes the form of a unidirectional slip pulse. Examples  
 365 are shown in Figure 7 for  $a/b = 0.8, 0.9, \text{ and } 0.95$ . The initial and boundary conditions  
 366 are identical for each panel; the direction of pulse propagation is presumably determined  
 367 by the initial heterogeneity. Except for the slip-weakening zone, over the region the pulse  
 368 has propagated the stress increases quasi-linearly with distance behind the propagating  
 369 front (Figure 7, row 3). Such a stress distribution is consistent with elasticity, in that it  
 370 represents a plausible smoothing of the  $1/r$  stress perturbation associated with a dislo-  
 371 cation. In conjunction with the friction law, such a stress distribution also requires that  
 372 the pulse accelerate to instability. To see this, consider a hypothetical steady-state pulse  
 373 with a stress distribution  $\tau(x')$  and slip distribution  $\delta(x')$  that are independent of time,

374 with  $x'$  being distance behind the tip. Then from the tail of the slip-weakening region to  
 375 the location of peak slip  $\dot{\tau}$  is positive, while  $V$ , always positive, is proportional to the slip  
 376 gradient  $\delta'$ , and  $\dot{V}$ , proportional to  $\delta''$ , is negative. With reference to equation (40), the  
 377 second term on the left (the  $b\dot{\theta}/\theta$  term) is negative when  $\Omega > 1$ , as for the examples in  
 378 Figure 7, and even if  $\Omega$  were less than 1 this term would be negligible near the peak slip,  
 379 as  $\delta'$  (that is,  $V$ ) approaches zero. The  $\dot{V}/V$  term, on the other hand, is negative wherever  
 380 the slip distribution is concave downward. Thus, equation (40) cannot be satisfied by a  
 381 steady-state pulse. For  $\dot{\tau}$  to be positive,  $\dot{V}$  must be positive, and this requires some com-  
 382 bination of an ever-increasing slip gradient or propagation speed, either of which implies  
 383 acceleration to instability.

384 Note that although these nucleation zones are certainly pulse-like in a practical sense,  
 385 they are not pulses in the strict sense of *Perrin et al.* [1995], who required  $V = 0$  at some  
 386 distance  $W$  behind the propagating front. *Freund* [1979] introduced slip pulses with a  
 387 velocity distribution of the form  $V(x') \propto [(W - x')/x']^{1/2}$ , where  $x'$  is distance from the  
 388 tip. Such pulses possess a discontinuity in  $dV/dx$  but no stress singularity at the healing  
 389 front ( $x' = W$ ). The pulses in Figure 7 are similar but possess a smoother “healing” front,  
 390 followed by an exponentially decaying tail. Within the tail the slip speed is low enough  
 391 that  $\dot{\theta}/\theta$  is negligible, and  $\dot{V}$  is determined by a local balance between  $a\dot{V}/V$  and the  
 392 positive  $\dot{\tau}/\sigma$  that comes from propagation at the tip.

#### 393 4.2.1. Pulse shape

394 In this section we use the estimated fracture energy to characterize the shape of the  
 395 pulse front; in the following we use this to estimate the propagation speed. Near a crack

tip but outside the slip-weakening zone,

$$\delta \approx \frac{4}{\sqrt{\pi}} \sqrt{\frac{G_c}{\mu'}} \sqrt{x'} \quad (46)$$

[Lawn, 1993]. Substituting the fracture energy from (45) and using the maximum slip speed  $V_{max}$  as the relevant velocity scale, (46) becomes

$$\frac{\delta}{D_c} \approx \frac{4}{\sqrt{\pi}} \left( \ln \frac{V_{max}\theta_i}{D_c} \right)^{1/2} \left( \frac{x'}{L_b} \right)^{1/2}. \quad (47)$$

That is, slip is expected to increase as the square-root of the distance behind the tip and to scale as  $[\ln(V_{max}\theta_i/D_c)]^{1/2}$ . Figure 8a shows  $\delta/D_c$  as a function of  $x'/L_b$  for all slip profiles in Figure 7 corresponding to  $V_{max} \geq 10^{-5}$  m/s (for  $a/b = 0.8$ ) and  $V_{max} \geq 10^{-6}$  m/s (for  $a/b = 0.9$  and  $0.95$ ). The propagating front is identified as the interpolated location of peak stress. Slip has been offset to zero at the front, and the slip profiles for  $a/b = 0.8$  and  $0.9$  have been reversed so that all the pulses apparently move to the left. As suggested by (47), Figure 8b further normalizes the slip by  $[\ln(V_{max}\theta_i/D_c)]^{1/2}$ , where  $\theta_i$  is the largely unperturbed value of  $\theta$  ahead of the propagating front. Whereas successive snapshots in Figure 8a increase in amplitude, the scaled profiles in Figure 8b decrease toward a relatively stable slip distribution over greater and greater distances behind the tip. The bold dashed curve shows the normalized slip estimate  $(4/\pi^{1/2})(x'/L_b)^{1/2}$  from (47). The close agreement with the numerical profiles near the propagating front indicates that the fracture energy estimated from (45) is appropriate despite the non-constant velocity behind the front.

415 In general, for a fracture tip propagating at equilibrium

$$416 \quad G_c = G \propto \Delta\tau^2 W, \quad (48)$$

417 where the stress drop  $\Delta\tau$  acts over the length scale  $W$ . We find that for the examples of  
 418 Figure 7 the fracture energy balance  $G_c \propto \ln(V_{max}\theta_i/D_c)$  is maintained by increasing  $\Delta\tau$   
 419 within the pulse approximately as  $\ln(V_{max}\theta_i/D_c)^{1/2}$  while the pulse width  $W$  (from tip  
 420 to maximum displacement) remains roughly constant (e.g., at  $\sim 5L_b$  for  $a/b = 0.95$  and  
 421  $\sim 1.5L_b$  for  $a/b = 0.9$ ). This is consistent with the slip amplitude increasing roughly as  
 422  $[\ln(V_{max}\theta_i/D_c)]^{1/2}$ , as in Figure 8b. Both the pulse width and slip amplitude increase as  
 423  $a/b$  approaches 1.

424 Despite the quasi-regular appearance of the velocity and slip profiles in Figures 7 and  
 425 8, we have thus far been unable to derive analytic approximations for the pulse width or  
 426 slip amplitude as functions of  $a/b$ . Related to this, perhaps, there is more than one style  
 427 of pulse capable of satisfying the fracture energy balance. Figure 9 shows examples where  
 428 the initial conditions consist of a locally peaked stress on an otherwise uniform surface,  
 429 subjected to a constant background loading rate. The simulations differ in  $a/b$  and in the  
 430 length scale of the initial stress perturbation. In Figure 9a, the slip amplitude remains  
 431 roughly constant while the front continually steepens (Figure 9c). In this case the fracture  
 432 energy balance is maintained by increasing  $\Delta\tau$  within the pulse as  $\sim \ln(V_{max}\theta_i/D_c)$  while  
 433  $W$  shrinks as  $\sim (\ln[V_{max}\theta_i/D_c])^{-1}$ . In Figure 9d, both the maximum slip and the pulse  
 434 width increase very nearly as  $\ln(V_{max}\theta_i/D_c)$ , so the slip pulse appears nearly self-similar  
 435 (Figure 9f). The fracture energy balance is maintained by increasing  $W$  as  $\sim \ln(V_{max}\theta_i/D_c)$

436 while  $\Delta\tau$  remains essentially unchanged. For all pulse styles, however, the near-tip slip  
 437 profile retains the scaling of equation (47) (Figure 8c).

438 These differences in style are necessarily sensitive to the ambient conditions along the  
 439 fault. For example, in Figure 7 (row 4) the minimum value of  $\Omega$  behind the pulse tip  
 440 is quasi-constant; this is also true of the example on the right in Figure 9 and, to a  
 441 slightly lesser extent, of the example on the left. We find also that the slip speeds at  
 442 these minima are a quasi-constant fraction of  $V_{max}$ . From the friction law this leads to  
 443  $d\tau_{min}/d(\ln V_{max}) \approx \text{constant}$ , where  $\tau_{min}$  is the stress minimum behind the tip (this occurs  
 444 very close to the location of the minimum  $\Omega$ ). But for  $d\tau_{min}/d(\ln V_{max}) \approx \text{constant}$  to be  
 445 consistent with values of  $\Delta\tau$  that scale as various powers of  $\ln(V_{max}\theta_i/D_c)$  (i.e., 0, 1/2, or  
 446 1) places requirements on the ambient stress. For example, for  $\Delta\tau$  to be independent of  
 447  $V_{max}$ , as for the quasi-self-similar simulation in Figure 9, the ambient stress must decrease  
 448 in parallel with  $d\tau_{min}/d(\ln V_{max})$ ; that this is the case can be seen in Figure 9g.

#### 449 4.2.2. Propagation velocity

450 Close examination of the slip profiles shows that the length  $R$  of the slip-weakening  
 451 region is shrinking. Dimensionally,

$$452 \quad R \sim \delta_c \frac{\mu'}{\Delta\tau_{p-r}} \quad (49)$$

453 [*Rice*, 1980], where  $\delta_c$  is the effective slip-weakening distance. Because  $\Delta\tau_{p-r}$  in-  
 454 creases roughly as  $\ln(V_{max}/V_{bg})$  while  $\delta_c$  is effectively fixed (Figure 1b),  $R$  decreases as  
 455  $[\ln(V_{max}/V_{bg})]^{-1}$ . In addition, because the stress profiles in Figure 1b are scaled versions  
 456 of one another, the location of any particular  $\delta \leq \delta_c$  scales by this same factor. This is  
 457 shown in Figures 10a and 10b by the extent to which the slip profiles superimpose when

458 the horizontal axis is stretched by  $\ln(V_{max}\theta_i/D_c)$ . Moreover, Figure 10e, which rescales all  
 459 the slip profiles of Figures 8b and 8c, shows that very near the tip this shape is universal.  
 460 The factor  $\ln(V_{max}\theta_i/D_c)$  here ranges from about 10 to more than 20. Thus, while the  
 461 scaling of equation (47) and Figure 10a applies on a length scale that is somewhat less  
 462 than the pulse width, on the still smaller scale of the slip-weakening region the scaling  
 463 of Figure 10b applies. This shrinking of the slip-weakening region is what necessitates a  
 464 very fine spatial grid to resolve slip-law nucleation fronts at large slip speeds.

465 We can formalize the above, and as a corollary estimate the pulse propagation velocity,  
 466 by writing that within the slip-weakening region

$$\frac{\delta(x, t)}{D_c} = s(\bar{x}) , \tag{50}$$

468 where  $s$  is a function of dimensionless scaled position  $\bar{x}$ , defined as

$$\bar{x} \equiv \frac{x'}{L_b} \ln \frac{V_{max}\theta_i}{D_c} , \tag{51}$$

470 with  $x'$  being distance behind the front. Differentiating with respect to time, the slip  
 471 speed is

$$\frac{V}{D_c} = \frac{ds}{d\bar{x}} \frac{d\bar{x}}{dt} = \frac{ds}{d\bar{x}} \left[ \frac{V_{prop}}{L_b} \ln \frac{V_{max}\theta_i}{D_c} + \bar{x} \frac{\dot{V}_{max}}{V_{max}} \left( \ln \frac{V_{max}\theta_i}{D_c} \right)^{-1} \right] , \tag{52}$$

473 where  $V_{prop}$  is the pulse propagation velocity and  $\dot{V}_{max} \equiv dV_{max}/dt$ . The first term in  
 474 brackets represents the contribution from the translation of a time-invariant slip profile,  
 475 and the second the contribution from a slip profile that steepens with time behind a  
 476 stationary tip (due to the increasing  $V_{max}$ ; in these examples  $\dot{\theta}_i/\theta$  is negligible compared  
 477 to  $\dot{V}_{max}/V_{max}$ ). The rate of increase of  $V_{max}$  is slow enough that in all our simulations the

478 slip speed is dominated, by at least 1–2 orders of magnitude, by the translation and not  
 479 the steepening of the front (Appendix B). Dropping the latter term and evaluating (52)  
 480 at  $V = V_{max}$  yields

$$481 \quad \frac{V_{prop}}{V_{max}} \approx 0.75 \frac{\mu'}{b\sigma} \left( \ln \frac{V_{max}\theta_i}{D_c} \right)^{-1}, \quad (53)$$

482 where the coefficient 0.75 is the inverse of  $ds/d\bar{x}$  taken from the numerical simulations at  
 483  $V = V_{max}$ , occurring at  $\bar{x} \sim 0.7$  (Figure 10).

484 Equation (53) suggests that  $V_{prop}$  increases with  $V_{max}$  but is independent of  $a/b$ . Thus,  
 485 the very different appearances of the pulses in Figure 7 are due not to slower propagation  
 486 with decreasing  $a/b$ , but to more rapid acceleration of slip (so that there is less time for  
 487 propagation, at the same  $V_{prop}$ , between neighboring slip speeds). This is confirmed in  
 488 Figure 11, which shows that plots of  $V_{prop}$  versus  $V_{max}$  for the 5 simulations in Figures  
 489 7 and 9 are indistinguishable once the pulse is well-developed. The values of  $\theta_i$  at the  
 490 conclusion of these simulations vary by a factor of  $\sim 10$ , but at large  $V_{max}\theta_i/D_c$  this  
 491 amounts to differences in the logarithmic factor of only 10%.

492 The essentials of equation (53) can be derived more transparently by starting with the  
 493 assumption of a time-invariant slip profile [e.g., *Ida, 1973*]. In this case the maximum slip  
 494 speed is given dimensionally by  $\delta_c/(R/V_{prop})$ , where the denominator is the time scale for  
 495 passage of the slip-weakening zone. Substituting (49) for  $R$  leads to

$$496 \quad \frac{V_{prop}}{V_{max}} \sim \frac{\mu'}{\Delta\tau_{p-r}} \sim \frac{\mu'}{b\sigma} \left( \ln \frac{V_{max}\theta_i}{D_c} \right)^{-1}. \quad (54)$$

497 For  $\mu' = 40$  GPa,  $\sigma = 40$  MPa,  $b = 10^{-2}$ , and the inverse logarithm of order  $10^{-1}$ ,  
 498  $V_{prop}/V_{max}$  is of order  $10^4$ . The middle expression in (54) shows that this result is inde-  
 499 pendent of the evolution law, as this affects only the path to steady state and not the

500 total strength drop. In Appendix B we generalize the more complete equations (50)–(53)  
 501 to fracture energies that scale as  $(\ln[V/V_{bg}])^n$ . By comparing the result for the aging  
 502 law to an estimate derived by differentiating the time-dependent nucleation length, we  
 503 gain insight into why, in the simulations of *Rubin and Ampuero* [2005a],  $V_{max}$  near the  
 504 margin of the nucleation zone becomes substantially larger than  $V$  in the interior as  $a/b$   
 505 approaches 1.

506 Equation (54) can also be used to judge whether the assumption of quasi-static elasticity  
 507 is violated sooner by locally high slip speeds or by propagation of the slip pulse at near  
 508 the shear wave speed. We can define  $V_{dyn}$  as the slip speed at which the local “radiation  
 509 damping” term,  $\dot{\tau}^{rad} = \dot{V}\mu/2c_s$  [*Rice*, 1993], becomes more important than the direct  
 510 velocity effect in equation (15); the result is  $V_{dyn} = 2a\sigma c_s/\mu$ , where  $c_s$  is the shear wave  
 511 speed. Substituting into (54) yields

$$\frac{V_{prop}/c_s}{V_{max}/V_{dyn}} \approx \frac{a}{b} \left( \ln \frac{V_{max}\theta_i}{D_c} \right)^{-1}. \quad (55)$$

513 Because the logarithm may exceed 20 by the time  $V_{max}$  approaches  $V_{dyn}$  (with  $D_c/\theta_i$   
 514 approximated as  $V_{plate}$  and  $V_{dyn}$  of order 0.1 m/s), we expect the applicability of quasi-  
 515 static elasticity to be limited by the magnitude of the local slip speed rather than the  
 516 propagation speed. Of course, other processes, such as frictional heating, may become  
 517 important at even lower speeds (e.g., *Segall and Rice* [2006]).

### 518 4.2.3. Time to instability

519 For the simulations of Figure 7, Figure 11 shows that plots of the time remaining to  
 520 instability ( $t^* - t$ ) vs.  $V_{max}$  have slopes that are indistinguishable from  $-1$ , implying  
 521  $\dot{V}_{max}/V_{max}^2 = \text{constant}$ , just as in both aging law regimes. These curves are offset such

522 that at the same  $V_{max}$  lower values of  $a/b$  reach instability sooner, as for the aging law.  
 523 Qualitatively, following the arguments of section 4.2, this is consistent with the larger  
 524 stress gradients behind the pulse tip for smaller  $a/b$  (Figure 7, row 3). That is, because  
 525 the pulse propagation speed at a given  $V_{max}$  is independent of  $a/b$ , a larger stress gradient  
 526 implies a larger  $\dot{\tau}$ , which in turn requires a larger  $\dot{V}/V$ .

527 For the simulation of Figure 9d,  $d(\ln V_{max})/dL = \text{constant}$  (the snapshots are plotted at  
 528 equal increments of  $\log V_{max}$  and show equal translations of the pulse front). Combining  
 529 this with (53) shows that for this simulation  $(\dot{V}_{max}/V_{max}^2) \ln(V_{max}\theta_i/D_c) = \text{constant}$ . For  
 530 the simulation of Figure 9a,  $(\dot{V}_{max}/V_{max}^2)[\ln(V_{max}\theta_i/D_c)]^{-1} \approx \text{constant}$ , reminiscent of the  
 531  $\Omega \gg 1$  regime for the slip law. Note, however, that unlike the aging law in both regimes  
 532 and the slip law for  $\Omega \gg 1$  there is no fixed point that accelerates in this fashion; the  
 533 point currently slipping at  $V_{max}$  has just been added to the pulse front.

534 Compared to the total duration of nucleation, the slip-law pulses may be short-lived.  
 535 For the simulation with  $a/b = 0.8$  in Figure 11,  $(t^* - t)$  is within 10% of  $D_c/V_{max}$ . Thus,  
 536 if the pulse develops at  $V_{max} \sim 10^{-6}$  m/s, as in Figure 7, it would persist for 400 s for  
 537  $D_c = 400 \mu\text{m}$  or 10 s for  $D_c = 10 \mu\text{m}$ . For the larger values of  $a/b$  in Figure 11, the pulses  
 538 begin at somewhat lower slip speeds and might last 10 – 100 times longer. Missing from  
 539 this analysis is a detailed understanding of how the initial conditions determine the slip  
 540 speed at the onset of pulse formation, although this is certainly related to the decrease  
 541 in  $\Omega$  in the interior of the nucleation zone. The potential importance of the pulses is  
 542 that they might be the only phase of quasi-static nucleation observable by near-source  
 543 instruments.

#### 544 4.2.4. “Nucleation length” in relation to the critical stiffness for instability

545 For the aging law, the region where the slip speed is well above background is more-or-  
546 less comparable to the region that is being elastically unloaded. This rough equivalence  
547 is generally assumed in any attempt to estimate the nucleation length from the critical  
548 stiffness of a spring-block slider. For the slip law in the near-steady-state regime, this  
549 equivalence breaks down. At any moment only the tip of the slip pulse is being unloaded,  
550 on a spatial scale that varies from about 6 to 9 times  $L_b/\ln(V_{max}\theta_i/D_c)$  as  $a/b$  varies from  
551 0.8 to 0.95.

552 The shrinking of the unloading region can also be viewed in terms of the competition  
553 between elasticity and slip-weakening. From equations (8) and (7), the instantaneous  
554 slip-weakening rate following a large step increase in sliding velocity is a constant  $b\sigma/D_c$   
555 for the aging law, but is larger than this by  $\ln(V_{max}\theta_i/D_c)$  for the slip law (Figure 1).  
556 The increase in slip weakening rate with increasing  $V_{max}$  is what promotes continued  
557 localization under the slip law. It is tempting to relate this also to the fact that slip-  
558 law spring-block sliders can reach instability for an arbitrarily large stiffness, given a  
559 sufficiently large perturbation from steady state [Gu *et al.*, 1984]. Such perturbations can  
560 of course be imposed externally, but Figures 7 and 9 show that they also arise naturally  
561 from nucleation itself, as the approaching slip pulse imposes a large stress perturbation  
562 on the fault immediately ahead. Once the slip-weakening zone passes by, this region  
563 continues to accelerate to instability (driven in part by the increasing stress due to slip  
564 near the current front), but much more slowly than the region at the front of the pulse  
565 where  $\Omega$  is extremely large. Something similar happens in the  $\Omega \gg 1$  regime, in that large  
566 values of  $\Omega$  arising spontaneously during nucleation allow the nucleation zone to shrink  
567 to sizes several times smaller than that anticipated from a linear stability analysis.

## 5. Relation to slow transients

568 Recently, periodic slow slip events have been identified near the base of the seismogenic  
 569 portion of subduction zones in Cascadia and southwest Japan [*Dragert et al.*, 2001; *Obara*  
 570 *and Hirose*, 2006]. Well-documented examples have total slips of  $\sim 1 - 2$  centimeters, ex-  
 571 tend several tens of kilometers down-dip, migrate along strike at rates of order 10 km/day,  
 572 and have periodicities of  $\sim 6 - 14$  months. These events are of interest both from a seismic  
 573 hazards standpoint and as a target for rate-and-state friction models. *Liu and Rice* [2005]  
 574 observed “slow slip events” near the seismic/aseismic transition in 3-D numerical simu-  
 575 lations using the aging law. The events were apparently constrained against instability  
 576 because of prior earthquakes that had ruptured the full extent of the seismogenic region.  
 577 The down-dip extent of the transition from fully velocity-weakening to velocity-neutral  
 578 behavior, about 5 km, was larger than both the fixed-length nucleation length  $2L_\nu$  and the  
 579 “classical” minimum length for instability  $L_{min}$ , but smaller than the asymptotic crack  
 580 length  $2L_\infty$  ( $\sim 10$  km even in the fully velocity-weakening region). In principle the for-  
 581 mer could allow for nucleation while the latter might prevent acceleration to instability.  
 582 For example, Perfetinni and Ampuero [ms in preparation] ran cycle simulations with a  
 583 velocity-weakening patch of length  $2L$  embedded in a larger velocity-strengthening re-  
 584 gion, driven by a constant far-field velocity. They observed “periodic slow slip events” for  
 585  $L_{min} \lesssim L \lesssim L_\infty$  and instability (maximum slip speed limited by radiation damping) for  
 586  $L \gtrsim L_\infty$ . Our own simulations (unpublished), using a geometry more akin to a subduction  
 587 zone (a velocity-weakening patch bordered by one locked and one velocity-strengthening  
 588 region, as was carried out previously by Liu and Rice [Spontaneous and triggered aseismic  
 589 deformation transients in a subduction fault model, manuscript submitted to J. Geophys.

590 Res., 2007]) indicate that the corresponding boundaries are closer to  $2L_{min}$  and  $2L_{\infty}$ .  
 591 Thus, the expected range of patch lengths large enough for nucleation but too small for  
 592 instability increases roughly in proportion to  $b/(b-a)$ , which becomes unbounded in the  
 593 limit of velocity-neutral slip. Similar behavior occurs also in simulations using slip law,  
 594 but over a much narrower range of patch lengths, as can be surmised from Figure 7.

595 The slow events in *Liu and Rice* [2005] had maximum slip speeds of  $\sim 10^{-8} - 10^{-7}$   
 596 m/s, roughly 1 – 2 orders of magnitude above background, and propagated along strike  
 597 at velocities of  $\sim 10^{-4} - 10^{-3}$  m/s. Thus the ratio  $V_{prop}/V_{max}$  was roughly  $10^4$ . The ratio  
 598  $\mu'/b\sigma$  at the propagating front was  $2 \times 10^4$ . For  $V_{max}\theta_i/D_c \sim 10^1 - 10^2$  the predicted  
 599 ratio  $V_{prop}/V_{max}$  from (54) is  $0.9 - 0.45 \times 10^4$ . This factor of 2 or so agreement could  
 600 be fortuitous, in that for slip speeds only 1 – 2 orders of magnitude above background  
 601 the near-tip slip profile might not yet have reached its asymptotic distribution, but it is  
 602 nonetheless encouraging.

603 To consider a natural example, the August 1999 Cascadia event had  $\sim 2$  cm of slip over  
 604 a down-dip extent of 50 km, and propagated  $\sim 300$  km at  $V_{prop} \sim 6$  km/day ( $\sim 0.07$  m/s)  
 605 [*Dragert et al.*, 2001]. The maximum slip speed is not well constrained. The geodetic  
 606 signal at individual GPS stations lasted from 6–15 days, yielding a nominal slip rate  
 607  $V \sim 2 \times 10^{-8}$  m/s (2 cm/ $10^6$  s), but if the slip speed were as peaked as for the slip-law  
 608 examples in this paper, or the aging-law examples with  $a/b \gtrsim 0.9$  in *Rubin and Ampuero*  
 609 [2005a], the peak value could be several times larger and for slip at 30–40 km depth would  
 610 likely be unresolved by surface stations. Arbitrarily multiplying the nominal value by 5  
 611 yields a maximum slip speed of  $V_{max} \sim 10^{-7}$  m/s, about  $10^2$  times the plate convergence  
 612 rate, and a ratio  $V_{prop}/V_{max}$  of  $\sim 0.7 \times 10^6$ . With  $\mu = 30$  GPa,  $b = 0.01$ , and  $V_{max}\theta_i/D_c$

613 approximated as the ratio of the slip rate to plate rate (the logarithm makes the result  
 614 rather insensitive to this estimate), equation (54) indicates that this ratio of  $V_{prop}/V_{max}$   
 615 implies an effective normal stress  $\sigma$  of 1 MPa. Although this is a very small value, it is  
 616 of the same order as that advocated by Liu and Rice [submitted manuscript] to match  
 617 the observed 14-month periodicity of the Cascadia events. They argue that such small  
 618 effective stresses might be produced by dehydration reactions in the subducting plate.

619 Other rate-and-state considerations point to low effective stresses as well. The  
 620 slip/length ratio is given by  $\delta/2L \sim \Delta\tau/\mu'$ ; to reach 2 cm of slip over a length scale  
 621 of 50 km requires a very low stress drop of 0.016 MPa for  $\mu' = 40$  GPa. Approximat-  
 622 ing the rate-and-state stress drop as  $\sigma(b - a) \ln(V/V_{bg})$ , and taking  $V/V_{bg} \approx 10^2$  and  
 623  $(b - a) \approx 10^{-3}$ , implies  $\sigma = 3.5$  MPa. Stabilizing slip over a patch size of tens of kilome-  
 624 ters is also aided by low values of  $\sigma$ , as all the relevant length scales are proportional to  
 625  $\sigma^{-1}$ . Using the aging law as an example, requiring  $4L_\infty \gtrsim 50$  km and taking  $b \approx 10^{-2}$ ,  
 626  $(b - a) \approx 10^{-3}$ , and  $D_c \approx 40 \mu\text{m}$  yields  $\sigma = 0.5$  MPa. While these three estimates of  
 627  $\sigma$  are not identical, they are encouragingly close, given their order-of-magnitude nature,  
 628 and uniformly low.

## 6. Which evolution law?

629 Neither the aging nor the slip law matches all the available laboratory friction data.  
 630 However, our simulations suggest that it is the behavior of the fault surface in the vicinity  
 631 of and well above steady state that controls nucleation, and here the slip law seems clearly  
 632 superior. *Nakatani* [2001] summarizes evidence that the effective slip-weakening distance  
 633 following a velocity increase does not increase with the magnitude of that increase. *Bayart*  
 634 *et al.* [2006] describe more recent experiments on synthetic quartz gouge showing that

635 velocity jumps of 1 and 2 orders of magnitude yield slip-weakening curves that are simply  
636 scaled version of one another, behavior that is consistent with the slip law but not the  
637 aging law (Figure 1). Even the general observation that it is more difficult to stabilize  
638 large velocity jumps than small jumps on velocity-weakening surfaces in the laboratory  
639 is consistent with a slip-weakening rate that increases with the magnitude of the velocity  
640 jump, behavior that is predicted by the slip law but not the aging law.

641 *Beeler et al.* [1994] found evidence for time-dependent, as opposed to slip-dependent,  
642 healing in slide-hold-slide experiments that access slip speeds and values of  $\Omega$  that are  
643 considerably smaller than those typical of velocity-stepping tests. Such behavior, which  
644 is inconsistent with the slip law, is likely to be important during the interseismic period.  
645 Except insofar as this influences the slip speed and the degree of heterogeneity along the  
646 fault as it passes through steady state from below, however, it is not apparent that this  
647 would significantly influence nucleation. Of the three relevant length scales that have been  
648 identified thus far —  $L_\nu$ ,  $L_{min}$  or  $h^*$ , and  $L_\infty$  — none make reference to behavior well  
649 below steady state. Rather, their analytic approximations depend upon the behavior well  
650 above steady state ( $L_\nu$ ), near steady state ( $L_{min}$ ), or a combination of well above steady  
651 state at the margins and near steady state in the interior ( $L_\infty$ ). If an evolution law that  
652 permits time-dependent healing during the interseismic period is desired for earthquake  
653 cycle simulations, ad-hoc approaches are available. These include the “composite” law of  
654 *Kato and Tullis* [2001], which combines the slip law with healing at low slip speeds, or  
655 a linear combination of the two laws with more weight attached to the slip law [*Sleep*,  
656 2005]. *Sleep* [2006] also presents micromechanical arguments outlining the conditions  
657 under which either the aging or slip law might apply.

## 7. Summary and conclusions

658 The slip and aging laws exhibit the same primary regimes of nucleation. Well above  
 659 steady state, when  $V\theta/D_c \gg 1$ , the two laws are qualitatively similar. Under the aging  
 660 law nucleation zones accelerate while maintaining a fixed length that is independent of  
 661  $a/b$ . Slip law nucleation zones are smaller than this by roughly  $\ln(V\theta/D_c)$ , and slowly  
 662 shrink as instability is approached. For both laws, however, laboratory values of  $a/b$  favor  
 663 nucleation near steady state, and here their behaviors differ markedly. This difference is  
 664 controlled by the behavior at the propagating front(s), which remain well above steady  
 665 state. That the fracture energy increases as  $[\ln(V/V_{bg})]^2$  for the aging law means that  
 666 nucleation takes the form of a quasi-statically expanding crack, whereas the increase as  
 667  $[\ln(V/V_{bg})]^1$  for the slip law gives rise to an accelerating slip pulse.

668 This difference is profound. For the aging law, with  $a/b = 0.95$ ,  $D_c = 100 \mu\text{m}$ , and an  
 669 effective normal stress of tens of MPa, the nucleation zone could be 1 km across, raising  
 670 the possibility that it could be observed remotely. For the slip law this seems unlikely, the  
 671 region of largest slip speeds being of order 100 times smaller. The smaller slip distances  
 672 during slip-law nucleation (e.g., Figure 2) also seem likely to make thermal pressurization  
 673 of pore fluid less important for the slip law than for the aging law [e.g., *Segall and Rice,*  
 674 2006].

675 Dropping the effective normal stress to  $\sim 1$  MPa, as advocated by Liu and Rice [sub-  
 676 mitted ms], could increase the aging law nucleation length to tens of kilometers. The  
 677 large disparity between  $L_\infty$  and either  $L_\nu$  or  $L_{min}$  for the aging law, particularly as  $a/b$   
 678 approaches 1, implies that there is a significant range of fault lengths capable of hosting

679 slow slip events; that is, fault lengths large enough for an event to nucleate but too small  
680 for it to reach instability.

681 Although for the slip law we have no analytical expression for a length scale compa-  
682 rable to  $L_\infty$ , our simulations suggest that the range of fault lengths permitting slow slip  
683 events for the slip law would be much less. By the same reasoning, any physical process  
684 that increases the effective fracture energy of the nucleation front with increasing slip  
685 speed more rapidly than  $(\ln[V/V_{bg}])^2$  would increase the range of fault lengths permitting  
686 such behavior. One plausible mechanism is inelastic dilation coupled with pore pressure  
687 reduction; because pore pressure recovery depends upon time and not slip, the effective  
688 slip-weakening distance in this case could increase quasi-linearly with slip speed, rather  
689 than logarithmically.

690 For both laws, migrating nucleation fronts have a ratio of propagation speed to maxi-  
691 mum slip speed of order  $(\mu'/b\sigma)(\ln[V_{max}/V_{bg}])^{-1}$ . The two velocities are related through  
692 the near-tip slip gradient, which is of order  $\Delta\tau_{p-r}/\mu'$ .

693 Three-dimensional simulations indicate a complete carry-over of the behaviors seen in  
694 2-D, with the slip-law pulses originating from either a mode-II or mode-III margin of the  
695 parent nucleation zone [Rubin and Ampuero, 2005b]. For the aging law, the transitional  
696 value of  $a/b$  in 3-D is  $\sim 0.195$ , roughly half that in 2-D, and for the slip law, with modest  
697 heterogeneity along the fault the transition seems to begin by  $a/b = 0.4$ . Thus, to the  
698 extent that laboratory evolution laws and rate-and-state parameters can be safely applied  
699 to the Earth, slip-law pulses might be the favored form of nucleation on natural faults. It  
700 must be borne in mind, however, that this requires extrapolation of experimental obser-  
701 vations to much larger velocity increases than have ever been achieved in the laboratory,

702 and that even within the range covered by experiment neither law satisfies all the data.  
 703 Our simulations demonstrate how remarkably different nucleation can appear using two  
 704 evolution laws that have each been advertised as “adequate” at some level.

### Appendix A: Stiffness of the expanding aging-law nucleation zone

705 That  $\Omega$  is quasi-constant in the interior of the growing aging-law nucleation zone implies  
 706 that the effective stiffness is a constant given by equation (35). The ability of the nucle-  
 707 ation zone to maintain (approximately) this stiffness even as it expands seems surprising,  
 708 but derives from the interaction of elasticity with the friction law, as outlined below.

709 Equation (36) for the stiffness at the center of a crack with a uniform stress drop can  
 710 be rewritten as

$$711 \quad k^* = \frac{\mu'}{2L} \left[ 1 + \frac{\Delta\tau \dot{L}}{\Delta\tau \dot{L}} \right]^{-1}. \quad (\text{A1})$$

712 Taking the logarithm of (29), which combines the criterion for equilibrium crack growth  
 713 with the aging-law estimates of  $\Delta\tau$  and  $\Delta\tau_{p-r}$ , and then differentiating leads to

$$714 \quad \frac{\Delta\tau \dot{L}}{\Delta\tau \dot{L}} = 2 \frac{\dot{\Delta\tau}_{p-r} \Delta\tau}{\Delta\tau_{p-r} \dot{\Delta\tau}} - 2. \quad (\text{A2})$$

715 With  $\Omega$  constant, equations (30) and (31) lead to

$$716 \quad \frac{\dot{\Delta\tau}_{p-r}}{\dot{\Delta\tau}} = \frac{b}{b-a}, \quad (\text{A3})$$

717 so (A2) becomes

$$718 \quad \frac{\Delta\tau \dot{L}}{\Delta\tau \dot{L}} = 2 \frac{b}{b-a} \frac{\Delta\tau}{\Delta\tau_{p-r}} - 2 = 2 \sqrt{\frac{L_\infty}{L}} - 2, \quad (\text{A4})$$

719 where the second equality makes use of the ratio  $\Delta\tau/\Delta\tau_{p-r}$  from (29) and (32). Substi-  
 720 tuting (A4) back into (A1), we obtain

$$721 \quad k^* = \frac{\mu'}{2L} \left[ 2\sqrt{\frac{L_\infty}{L}} - 1 \right]^{-1}. \quad (\text{A5})$$

722 This function has a broad minimum at  $L = L_\infty$ , implying that  $k^*$  remains close to  $\mu'/2L_\infty$   
 723 even for  $L/L_\infty$  considerably less than 1 (Figure 12a).

724 That  $\Omega$  remains quasi-constant all the way to the slip-weakening zone implies that  $k^*$   
 725 remains close to  $\mu'/2L_\infty$  over this entire region as well. For a stationary crack, the stiffness  
 726 near the margins is greater than that at the center (the slip is less for a given stress drop),  
 727 but propagation decreases the stiffness at the ends more than that at the center and these  
 728 two effects tend to cancel. From equation (28) of *Rubin and Ampuero* [2005a], the slip  
 729 speed within a growing crack subjected to a uniform but time-varying stress drop is

$$730 \quad V(x) = -\frac{2}{\mu'} \left[ \dot{\Delta\tau} L \left( 1 - \frac{x^2}{L^2} \right)^{1/2} + \Delta\tau \dot{L} \left( 1 - \frac{x^2}{L^2} \right)^{-1/2} \right]. \quad (\text{A6})$$

731 Dividing by  $\dot{\Delta\tau}$  and making use of (A4) leads to

$$732 \quad k^*(x) = -\frac{\mu'}{2L_\infty} \left[ \frac{L}{L_\infty} \left( 1 - \frac{x^2}{L^2} \right)^{1/2} + 2 \left( \sqrt{\frac{L}{L_\infty}} - \frac{L}{L_\infty} \right) \left( 1 - \frac{x^2}{L^2} \right)^{-1/2} \right]^{-1}, \quad (\text{A7})$$

733 where the bracketed expression now represents the deviation of the stiffness from the value  
 734 needed to maintain the given  $\Omega$ . Figure 12b plots this expression as a function of  $x/L_\infty$   
 735 for 4 values of  $L/L_\infty$ : 0.25, 0.5, 0.75, and 1. The curve for  $L/L_\infty = 1$  shows the increase  
 736 in  $k^*$  near the margins of a stationary crack, while the others show the decrease near the  
 737 margins of a propagating crack. The solid symbols indicate a distance of  $L_b$  behind the  
 738 crack tip for  $a/b = 0.8$  (triangles) and 0.9 (squares); (A7) is not expected to be accurate

739 closer to the tip than this because of the nonuniform stresses within the slip-weakening  
 740 region, which (A6) neglects. The tendency for points interior to this to plot near unity  
 741 is indicative of the ability of the crack to maintain a near-constant and uniform stiffness  
 742 as it grows. That this ability deteriorates as  $L/L_\infty$  approaches 1, especially for larger  
 743  $a/b$ , may explain much of the complexity seen in the simulations of *Rubin and Ampuero*  
 744 [2005a]. This complexity increased with both  $a/b$  and  $L/L_\infty$ .

745 Equation (33) of *Ranjith and Rice* [1999] can be rewritten to show that the trajectory  
 746  $\Omega = \text{constant}$  marks the stability boundary for a spring-block slider with zero load point  
 747 velocity. In light of this, the above considerations suggest what might happen when a  
 748 growing aging law nucleation zone encounters barriers spaced more closely than  $2L_\infty$ .  
 749 Because it can no longer expand and  $L < L_\infty$ , the nucleation zone stiffness will exceed  
 750 the critical value needed to maintain the current  $\Omega$ . It will then follow a trajectory of lesser  
 751 acceleration than the  $\Omega = \text{constant}$  case and (ultimately) deceleration to slip speeds low  
 752 enough that the background loading rate again becomes important. For some of the initial  
 753 and boundary conditions examined by *Rubin and Ampuero* [2005a], the nucleation zone  
 754 reached elastodynamic speeds before  $L$  reached  $L_\infty$ . However, for the cycle simulations of  
 755 Perfetinni and Ampuero [manuscript in preparation], with a velocity-weakening region of  
 756 length  $2L$  embedded in velocity-strengthening surroundings, elastodynamic speeds were  
 757 not reached except for  $L > L_\infty$ .

## Appendix B: Velocity of the nucleation front

758 Here we generalize the expression for  $V_{prop}/V_{max}$  to fracture energies that scale as  
 759  $(\ln[V/V_{bg}])^n$ , and discuss the implications of two independent estimates of  $V_{prop}$  for the  
 760 aging law. We continue to assume that the total strength drop is independent of the

761 evolution law, so

$$762 \quad \Delta\tau_{p-r} = b\sigma \ln \frac{V_{max}\theta_i}{D_c}, \quad (B1)$$

763 but allow for different slip-weakening distances

$$764 \quad \delta_c = \Pi D_c \left( \ln \frac{V_{max}\theta_i}{D_c} \right)^{n-1}, \quad (B2)$$

765 where  $\Pi$  is some constant coefficient (e.g., 1 for the aging law, for which  $n = 2$ ). We

766 assume that within this slip distance  $\Delta\tau/\Delta\tau_{p-r}$  is a function only of  $\delta/\delta_c$  (as is strictly

767 true for the slip law [ $n = 1$ ], and true for the aging law while  $\Omega \gg 1$ ). From equation

768 (49), the length of the slip-weakening zone is

$$769 \quad R = \alpha \Pi L_b \left( \ln \frac{V_{max}\theta_i}{D_c} \right)^{n-2}, \quad (B3)$$

770 where the coefficient  $\alpha$  depends upon the functional form of  $\Delta\tau/\Delta\tau_{p-r}$ ; for linear slip-

771 weakening, as for the aging law,  $\alpha \sim 0.7$ .

772 Provided the requirement of a small slip-weakening zone is met, equations (B2) and

773 (B3) lead to

$$774 \quad \frac{\delta(x, t)}{D_c} = A(t) s(\bar{x}), \quad (B4)$$

775 with

$$776 \quad A(t) \equiv \left( \ln \frac{V_{max}\theta_i}{D_c} \right)^{n-1}; \quad \bar{x} \equiv \frac{x'}{L_b} \left( \ln \frac{V_{max}\theta_i}{D_c} \right)^{2-n}; \quad (B5)$$

777 where  $x'$  is distance behind the tip, so  $0 \leq s \leq \Pi$  and  $0 \leq \bar{x} \leq \alpha\Pi$ . Differentiating (B4),

$$778 \quad \frac{V}{D_c} = \dot{A}s + A \frac{ds}{d\bar{x}} \frac{d\bar{x}}{dt}. \quad (B6)$$

779 Evaluating this at  $V = V_{max}$  and neglecting  $\dot{\theta}_i/\theta_i$  in relation to  $\dot{V}_{max}/V_{max}$ ,

$$\begin{aligned}
 780 \quad 1 &= (n-1) \left( \ln \frac{V_{max}\theta_i}{D_c} \right)^{n-2} \left( \frac{D_c \dot{V}_{max}}{V_{max}^2} \right) s(\bar{x}_m) \\
 781 \quad &+ \frac{ds}{d\bar{x}_m} \left[ \frac{V_{prop} \mu'}{V_{max} b\sigma} \left( \ln \frac{V_{max}\theta_i}{D_c} \right) + (2-n)\bar{x}_m \left( \frac{D_c \dot{V}_{max}}{V_{max}^2} \right) \left( \ln \frac{V_{max}\theta_i}{D_c} \right)^{n-2} \right], \quad (B7) \\
 782
 \end{aligned}$$

783 where  $\bar{x}_m$  denotes the location of  $V = V_{max}$  and  $ds/d\bar{x}_m$  the slope at that point. The  
 784 first term in brackets on the right represents the contribution from the translation of a  
 785 time-invariant slip profile; when this term dominates, equation (54) is recovered ( $ds/d\bar{x}_m$   
 786 is of order  $\alpha^{-1}$ ). The first term on the right, equal to zero for the slip law, is due to the  
 787 increasing amplitude of slip within slip-weakening zone. The second term within brackets,  
 788 zero for the aging law, comes from the steepening of the slip gradient due to shrinking of  
 789 the slip-weakening zone. For the slip law simulations of Figure 7, we find empirically that  
 790  $(D_c \dot{V}_m/V_{max}^2)$  is constant and decreases from 0.9 to 0.05 as  $a/b$  increases from 0.8 to 0.95.  
 791 As  $\bar{x}_m ds/d\bar{x}_m \sim 0.9$ , this term contributes less than 10% of the total for  $V_{max}\theta_i/D_c > 10^4$ ,  
 792 even for the smaller  $a/b$ .

793 For the aging law, note that because both  $\Delta\tau_{p-r}$  and  $\delta_c$  increase linearly with  
 794  $\ln(V_{max}/V_{bg})$ ,  $R$  is time-invariant (equation 49). For the aging-law simulation of Fig-  
 795 ure 3, Figure 13b superimposes the stresses near the rightmost tip for the 19 snapshots  
 796 shown in Figure 13a, scaled to vary from a peak value of 1 at the tip to 0 at the center  
 797 of the nucleation zone. For  $V_{max}/V_{bg} \gtrsim 10^3 - 10^4$  the length of the slip weakening zone  
 798 asymptotically approaches  $\sim 0.75L_b$ . Substituting the aging-law fracture energy into (46),  
 799 the equivalent of equation (47) for the slip profile of the propagating front is

$$800 \quad \frac{\delta}{D_c} \approx \sqrt{\frac{8}{\pi}} \left( \ln \frac{V_{max}\theta_i}{D_c} \right) \left( \frac{x'}{L_b} \right)^{1/2}. \quad (B8)$$

801 Figure 13e shows  $\delta/D_c$  divided by  $\ln(V_{max}\theta_i/D_c)$  as a function of distance behind the  
 802 propagating front, for the same 19 snapshots. The solid lines show the right tip, the  
 803 dashed lines the left (reversed for comparison), and the thick dashed line the estimate  
 804  $(8/\pi)^{1/2}(x'/L_b)^{1/2}$  from (B8). As suggested by Figure 13b, after about the 4th snapshot  
 805 the normalized slip asymptotically approaches the same distribution. Outside the slip-  
 806 weakening region, the dashed line provides a good fit to the slip profiles if it is shifted  
 807 to intersect the horizontal axis near the center of the slip-weakening region. Within the  
 808 slip-weakening region, the scaling of the axes shows that the fracture energy requirements  
 809 are satisfied by increasing the slip amplitude over a fixed length scale, rather than (as for  
 810 the slip law) by reaching the same slip over an ever-diminishing length scale.

811 Figures 13c and 13d indicate that for the aging law  $\bar{x}_m \sim 0.5$ ,  $s(\bar{x}_m) \sim 0.6$  and  $ds/d\bar{x}_m \sim$   
 812 1.6. Inserting these values and  $n = 2$  into (B7) leads to

$$\frac{V_{prop}}{V_{max}} \approx 0.6 \left( 1 - 0.6 D_c \frac{\dot{V}_{max}}{V_{max}^2} \right) \frac{\mu'}{b\sigma} \left( \ln \frac{V_{max}\theta_i}{D_c} \right)^{-1}. \quad (\text{B9})$$

814 Noting that the slip speed is quasi-uniform over the interior of the nucleation zone, we  
 815 might approximate  $\dot{V}_{max}/V_{max}^2$  as  $\dot{V}/V^2$ , so from (33) and (37), (B9) becomes

$$\frac{V_{prop}}{V_{max}} \approx 0.6 \left( 1 - 0.6 \frac{\pi}{2} \frac{b-a}{b} \right) \frac{\mu'}{b\sigma} \left( \ln \frac{V_{max}\theta_i}{D_c} \right)^{-1}. \quad (\text{B10})$$

817 The “1” within the parentheses represents the relative contribution from propagation  
 818 of a time-invariant slip profile, while the term proportional to  $(b-a)/b$  represents the  
 819 relative contribution from the increasing slip amplitude. The latter approaches zero as  
 820  $a/b$  approaches 1. Because  $0.6\pi/2 \sim 1$ , the entire coefficient in parentheses is very nearly  
 821  $a/b$ .

822 The ascending curves in Figure 14 show  $V_{prop}$  vs.  $V_{max}$  for the two ends of the nucleation  
 823 zone in Figure 13, starting from when the zone begins to expand. Note that the factor  
 824 of  $\sim 2$  difference in  $V_{prop}$  is almost entirely accounted for by a comparable difference in  
 825  $V_{max}$  behind the fronts, a difference that presumably is controlled by the heterogeneous  
 826 conditions along the fault. Similar behavior is seen in Figure 9d of Rubin and Ampuero,  
 827 where the difference between the fronts is closer to an order of magnitude. Note also  
 828 that the curves in Figure 14 are nearly identical to those of Figure 11 for the slip law, as  
 829 predicted by the similar coefficients in (B10) and (53). The horizontal curves in Figure  
 830 14 show  $V_{prop}$  normalized by the prediction of (B10); the agreement is quite good.

831 It should be noted that the aging-law propagation velocity can also be estimated by dif-  
 832 ferentiating the expression for the time-dependent nucleation length. Inserting equations  
 833 (30) and (31) into (29) leads to

$$834 \quad L = \frac{L_b}{\pi} \left( \frac{b}{b-a} \right)^2 \left[ \frac{\ln \frac{V \theta_i}{D_c} - \ln \Omega}{\ln \frac{V}{V_{bg}} - \frac{b}{b-a} \ln \Omega} \right]^2, \quad (\text{B11})$$

835 where  $V$  is the quasi-uniform slip speed within the nucleation zone,  $\theta_i$  is the relatively  
 836 unperturbed value of  $\theta$  ahead of the propagating front, and  $V_{bg}$  is the hypothetical sliding  
 837 velocity that at steady state would give rise to the ambient stress (that which would  
 838 act in the absence of the nucleation displacements). The bracketed term asymptotically  
 839 approaches 1 in the limit of large  $V$ . We find that in our simulations it approaches this  
 840 value from below, so that  $L$  approaches  $L_\infty$  from below, but we are unsure how general  
 841 this result is.

842 As  $\dot{L} = V_{prop}$  for symmetric growth, differentiating (B11) and using (33) and (37) for  
 843  $\dot{V}/V^2$  leads to

$$844 \quad \frac{V_{prop}}{V} = \frac{b}{b-a} \left[ \ln \left( \frac{D_c}{V_{bg}\theta_i} \right) - \frac{a}{b-a} \ln \Omega \right] \frac{\mu'}{b\sigma} \sqrt{\frac{L}{L_\infty}} \left( \ln \frac{V}{V_{bg}} \right)^{-2}. \quad (\text{B12})$$

845 This expression differs from equation (B10) for  $V_{prop}/V_{max}$  by the leading coefficient (in-  
 846 cluding the  $a/b$  terms) and an extra  $(\ln[V\theta_i/D_c])^{-1}$ . To some extent these differences can  
 847 be accommodated by modest differences between  $V$  and  $V_{max}$ , as seen in our aging-law  
 848 simulations. Comparing (B12) and (B10) leads to

$$849 \quad \frac{V}{V_{max}} \approx 0.6 \frac{a}{b} \left( 1 - \frac{a}{b} \right) \left[ \ln \left( \frac{D_c}{V_{bg}\theta_i} \right) - \frac{\pi}{2} \right]^{-1} \sqrt{\frac{L_\infty}{L}} \ln \frac{V}{V_{bg}}, \quad (\text{B13})$$

850 where we have evaluated the relatively insignificant term  $a \ln \Omega / (b - a)$  in the limit as  
 851  $a/b$  approaches 1. The  $(1 - a/b)$  term shows that, at fixed  $L/L_\infty$  and  $\ln(V/V_{bg})$ ,  $V_{max}/V$   
 852 increases strongly as  $a/b$  approaches 1, which qualitatively is consistent with Figures 9a  
 853 and 10 of *Rubin and Ampuero* [2005a] and other unpublished results in which  $V_{max}/V$   
 854 increases, during the crack-expansion phase of nucleation, from maximum values of  $\sim 1.1$   
 855 for  $a/b = 0.7$ , to  $\sim 1.5$  for  $a/b = 0.8$ , to  $\sim 6$  for  $a/b = 0.9$ , and to  $\sim 14$  for  $a/b = 0.95$ .

## 856 **Acknowledgments.**

857 Jim Dieterich suggested running the far-below-steady-state simulation of Figure 4. Sup-  
 858 ported by NSF grants EAR-0126184 and EAR-0538156. AR gratefully acknowledges a  
 859 Cox visiting professorship at Stanford University.

## References

- 860 Bayart, E., A. M. Rubin, and C. Marone (2006), Evolution of fault friction following large  
861 velocity jumps, *Eos Trans, AGU*, 87(52), Fall Meet. Suppl., Abstract S31A-0180.
- 862 Beeler, N. M., T. E. Tullis, and J. D. Weeks (1994), The roles of time and displacement  
863 in the evolution effect in rock friction, *Geophys. Res. Lett.*, 21, 1987–1990.
- 864 Blanpied, M. L., C. J. Marone, D. A. Lockner, J. D. Byerlee, and D. P. King (1998),  
865 Quantitative measure of the variation in fault rheology due to fluid-rock interactions,  
866 *J. Geophys. Res.*, 103, 9691–9712.
- 867 Dieterich, J. H. (1992), Earthquake nucleation on faults with rate- and state-dependent  
868 friction, *Tectonophys.*, 211, 115–134.
- 869 Dieterich, J. H., and B. D. Kilgore (1994), Direct observation of frictional contacts: New  
870 insights for state-dependent properties, *Pageoph.*, 143, 283–302.
- 871 Dieterich, J. H., and B. D. Kilgore (1996), Implications of fault constitutive properties for  
872 earthquake prediction, *Proc. Natl. Acad. Sci. USA*, 93, 3787–3794.
- 873 Dragert, H., K. Wang, and T. S. James (2001), A silent slip event on the deeper cascadia  
874 subduction interface, *Science*, 292, 1525–1528.
- 875 Freund, L. B. (1979), The mechanics of dynamic shear crack propagation, *J. Geophys.*  
876 *Res.*, 84, 2199–2209.
- 877 Gu, J.-C., J. R. Rice, A. L. Ruina, and S. T. Tse (1984), Slip motion and stability of a  
878 single degree of freedom elastic system with rate and state dependent friction, *J. Mech.*  
879 *Phys. Solids*, 32, 167–196.
- 880 Ida, Y. (1973), Maximum acceleration of seismic ground motion, *Bull. Seism. Soc. Am.*,  
881 63, 959–968.

- 882 Kato, N., and T. E. Tullis (2001), A composite rate- and state-dependent law for rock  
883 friction, *Geophys. Res. Lett.*, *28*, 1103–1106.
- 884 Kilgore, B. D., M. L. Blanpied, and J. H. Dieterich (1993), Velocity dependent friction of  
885 granite over a wide range of conditions, *Geophys. Res. Lett.*, *20*, 903–906.
- 886 Lawn, B. (1993), *Fracture of Brittle Solids - 2nd edition*, Cambridge University Press,  
887 Cambridge.
- 888 Liu, Y., and J. R. Rice (2005), Aseismic slip transients emerge spontaneously in three-  
889 dimensional rate and state modeling of subduction earthquake sequences, *J. Geophys.*  
890 *Res.*, *110*, B08307, doi:10.1029/2004JB003424.
- 891 Marone, C. (1998), Laboratory-derived friction laws and their application to seismic fault-  
892 ing, *Ann. Rev. Earth Planet. Sci.*, *26*, 643–646.
- 893 Nakatani, M. (2001), Conceptual and physical clarification of rate and state friction:  
894 Frictional sliding as a thermally activated rheology, *J. Geophys. Res.*, *106*, 13,347–  
895 13,380.
- 896 Obara, K., and H. Hirose (2006), Non-volcanic deep low-frequency tremors accompanying  
897 slow slips in the southwest japan subduction zone, *Tectonophys.*, *417*, 33–51.
- 898 Perrin, G., J. R. Rice, and G. Zheng (1995), Self-healing slip pulse on a frictional surface,  
899 *J. Mech. Phys. Solids*, *43*, 1461–1495.
- 900 Ranjith, K., and J. R. Rice (1999), Stability of quasi-static slip in a single degree of  
901 freedom elastic system with rate and state dependent friction, *J. Mech. Phys. Sol.*, *47*,  
902 1207–1218.
- 903 Rice, J. R. (1980), The mechanics of earthquake rupture, in *Physics of the Earth's Interior*,  
904 *Proc. Int. Sch. Phys. Enrico Fermi*, vol. 78, edited by A. M. Dziewonski and E. Boschi,

905 pp. 555–649.

906 Rice, J. R. (1993), Spatio-temporal complexity of slip on a fault, *J. Geophys. Res.*, *98*,  
907 9885–9907.

908 Rice, J. R., N. Lapusta, and K. Ranjith (2001), Rate- and state-dependent friction friction  
909 and the stability of sliding between elastically deformable solids, *J. Mech. Phys. Sol.*,  
910 *49*, 1865–1898.

911 Rubin, A. M., and J.-P. Ampuero (2005a), Earthquake nucleation on (aging) rate and  
912 state faults, *J. Geophys. Res.*, *110*, B11312, doi:10.1029/2005JB003686.

913 Rubin, A. M., and J.-P. Ampuero (2005b), 3-D earthquake nucleation on rate-and-state  
914 faults, *Eos Trans, AGU*, *86*(52), Fall Meet. Suppl., Abstract T13E-07.

915 Ruina, A. (1983), Slip instability and state variable friction laws, *J. Geophys. Res.*, *88*,  
916 10,359–10,10,370.

917 Segall, P., and J. R. Rice (2006), Does shear heating of pore fluid contribute to earthquake  
918 nucleation?, *J. Geophys. Res.*, *111*, B11312, doi:10.1029/2005JB004129.

919 Sleep, N. H. (2005), Physical basis of evolution laws for rate and state friction, *Geochem.*  
920 *Geophys. Geosyst.*, *6*, Q11008, doi:10.1029/2005GC000991.

921 Sleep, N. H. (2006), Real contacts and evolution laws for rate and state friction, *Geochem.*  
922 *Geophys. Geosyst.*, *7*, Q08012, doi:10.1029/2005GC001187.

**Table 1.** Notation

Parameter	Description
$a; b$	Coefficients of the rate-and-state direct and evolution effects
$C_{\Omega \gg 1}$	Coefficient of fixed-length nucleation (eqs. 19 & 23)
$C_{\Omega \sim 1}$	Coefficient of crack-like nucleation (eqs. 33 & 37)
$C'$	Coefficient of slip-law nucleation (eq. 42)
$D_c$	Characteristic slip distance in the evolution law
$G$	Energy release rate
$G_c$	Fracture energy
$h^*$	Classical estimate of the nucleation length (eq. 11)
$k; k^*$	Stiffness; effective crack stiffness
$k_{cr}$	Critical stiffness for instability
$L$	Half-length of the nucleation zone
$L_b$	Dieterich nucleation length scale (eq. 12)
$L_\nu$	Fixed nucleation half-length (eq. 22)
$L_{min}$	Minimum nucleation half-length (eq. 11)
$L_\infty$	Asymptotic nucleation half-length (eq. 32)
$R$	Length of the slip-weakening region
$t^*$	Time of instability
$V$	Slip speed
$V_{bg}$	Slip speed that at steady-state would give rise to the ambient shear stress
$V_{max}$	Maximum slip speed behind the propagating front
$V_{prop}$	Propagation speed of the nucleation front
$W$	Width of the slip-law pulse (tip to peak slip)
$x'$	Distance behind the propagating front
$\delta$	Slip distance
$\delta_c$	Critical slip distance in fracture energy expression
$\Gamma$	$\ln(V_{max}\theta_i/D_c)$ ; proportional to $\Delta\tau_{p-r}$
$\theta$	State variable in rate-and-state friction
$\theta_i$	Value of $\theta$ ahead of the propagating front
$\mu'$	$\mu$ (anti-plane strain) or $\mu/(1 - \nu)$ (plane strain), where $\mu$ is shear modulus and $\nu$ is Poisson's ratio
$\Omega$	$V\theta/D_c$ ; a measure of proximity to steady state
$\sigma$	Normal stress
$\tau$	Shear stress
$\tau^\infty$	Shear stress that would act in the absence of slip
$\Delta\tau$	Average stress drop in the nucleation zone
$\Delta\tau_{p-r}$	Strength drop at the propagating front

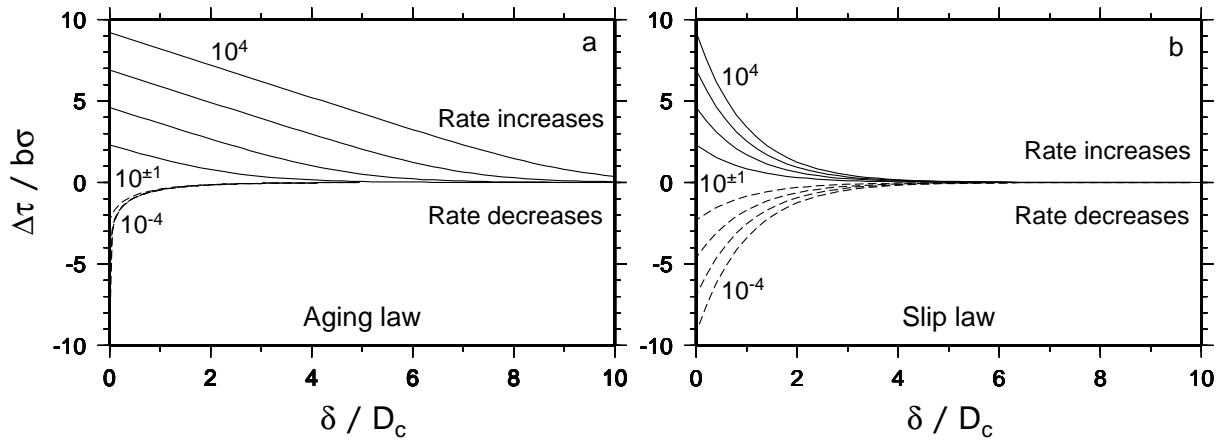


**Figure 1.** Plots of normalized stress as a function of normalized slip, for step velocity increases (solid lines) and decreases (dashed lines) of 1 – 4 orders of magnitude, for (a) the aging law and (b) the slip law. Stresses are relative to the future steady-state value. For the aging law the curves for step decreases of 2 – 4 orders of magnitude appear indistinguishable, but they intersect the vertical axis at the same values of  $\Delta\tau$  as for the slip law.

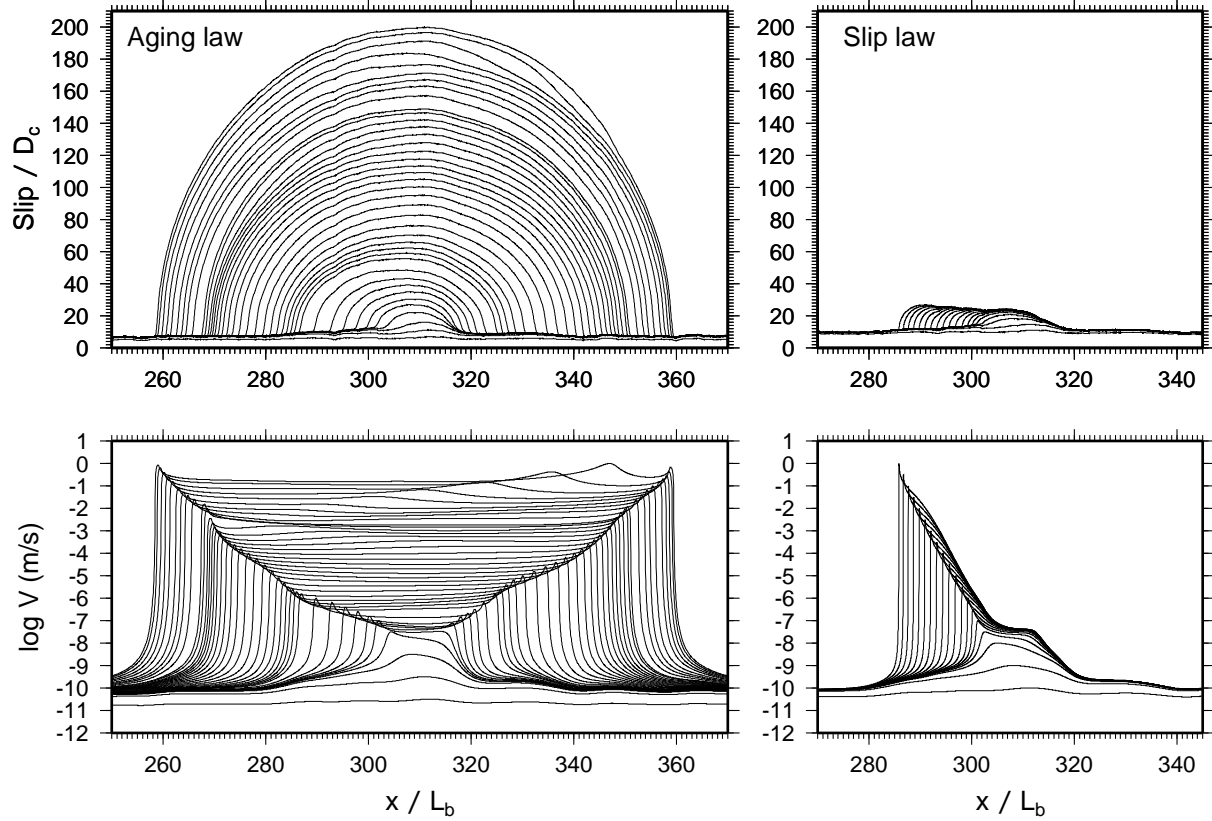


**Figure 2.** Snapshots of normalized slip (top panels) and slip speed (bottom) for two simulations identical in all respects except that the left panels use the aging law and the right panels the slip law.  $a/b = 0.95$ . The normalizing length scale  $L_b \equiv \mu' D_c / b \sigma$ . The grid spacing is  $L_b / 74$ ; initial and boundary conditions and material parameters are otherwise identical to those in Figure 3.

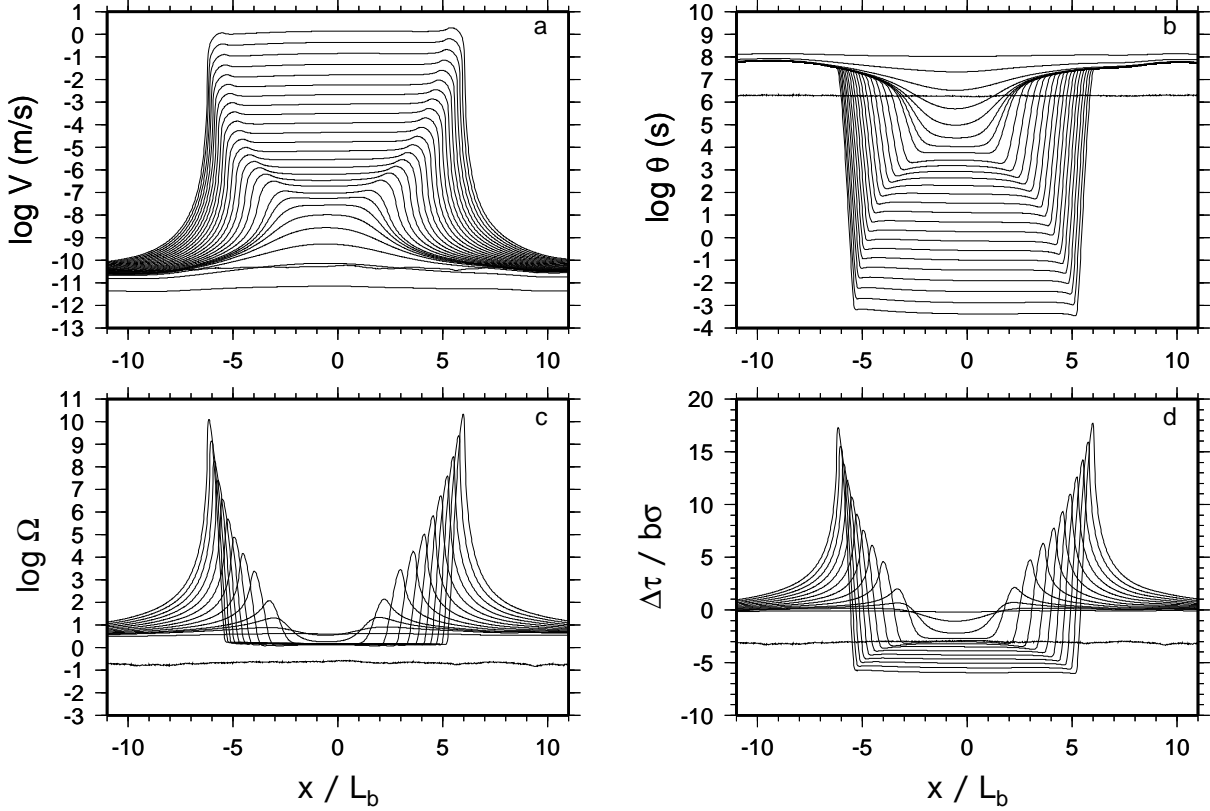


**Figure 3.** Snapshots from a simulation with a uniform initial slip speed of  $10^{-9}$  m/s, an initial  $\Omega$  randomly distributed between 0 and 1 on a grid spacing of 0.1 m ( $\sim L_b/46$ ), and  $\dot{\tau}^\infty = 10^{-2}$  Pa s $^{-1}$ .  $a/b = 0.8$ . (a) Slip speed, (b) state, (c)  $V\theta/D_c$ , and (d) normalized stress change from the far-field average; for clarity (c) and (d) show only every other profile. Note that while the nucleation zone expands these quantities are quasi-uniform in the interior, that  $\Omega$  is quasi-constant as well, and that  $\theta$  is not much perturbed until the arrival of the peak stress.

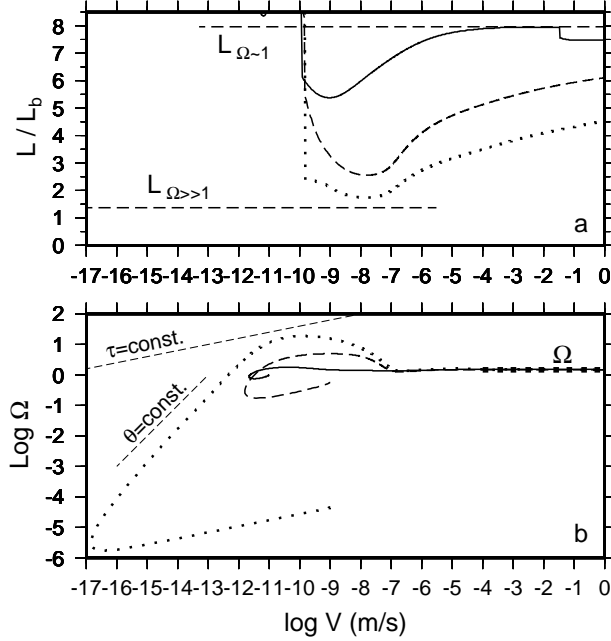


**Figure 4.** (a) Normalized nucleation length, defined as half the distance between the peaks in elastic stressing rate, and (b)  $\log(V\theta/D_c)$ , as functions of slip speed for 3 simulations with  $a/b = 0.8$ . The overall trend is for slip speed to increase with time. Dashed curve is for the simulation of Figure 3; dotted curve is for the identical conditions but with the initial  $\Omega$  reduced by 4 orders of magnitude; solid curve is for a peaked load on an otherwise uniform surface initially slightly below steady state. The dashed and dotted lines labeled  $L_\infty$  and  $\Omega$  refer to the predicted values for this  $a/b$  from equations (32) and (37). Note that  $\Omega$  matches the prediction even for  $L/L_\infty < 0.5$ , reflecting the near-constant stiffness in (36). In (b), the upper and lower dashed lines parallel trajectories of constant stress and state, respectively.

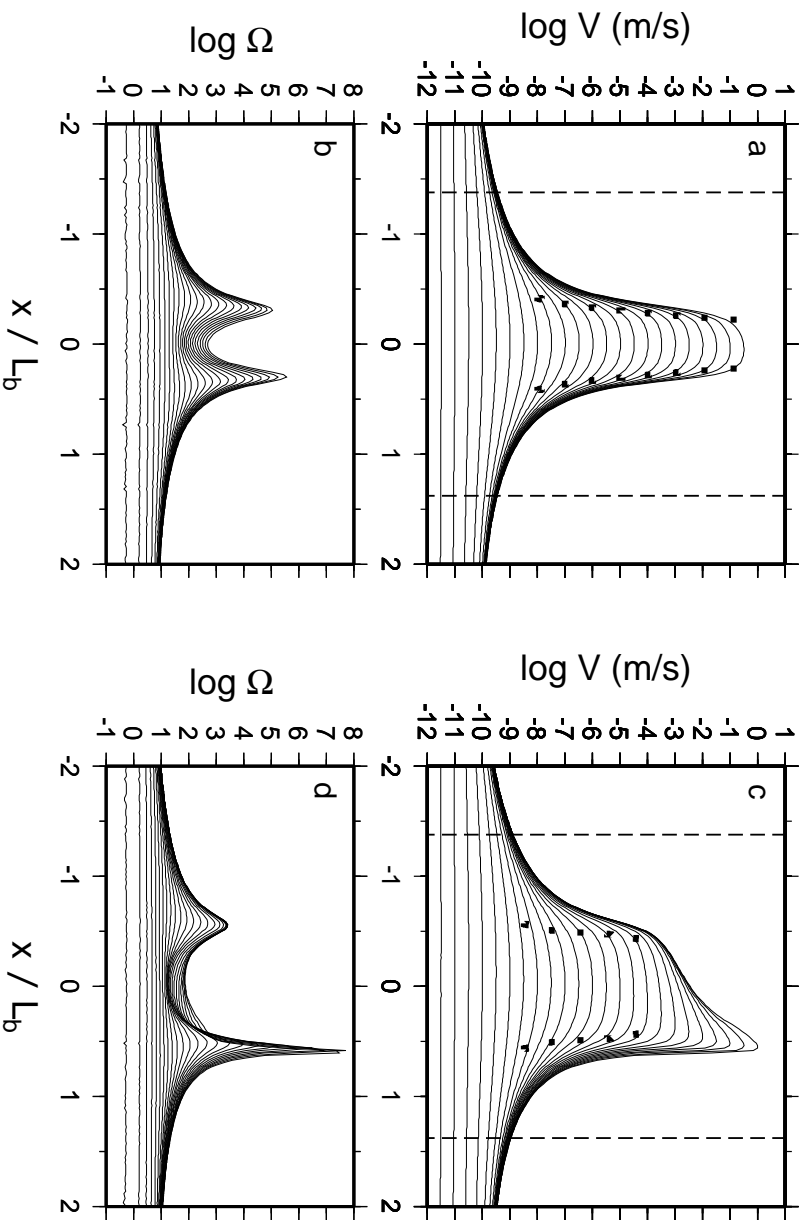


**Figure 5.** (a) and (b), Snapshots of slip speed and  $V\theta/D_c$  from a slip-law simulation with  $a/b = 0.5$ ; all other conditions are identical to those in Figure 3. Vertical dashed lines in (a) indicate the nucleation length from the aging-law fixed length solution. The dotted lines are smaller by  $\ln(\Omega)$ , with  $\Omega$  evaluated in the center of the nucleation zone. (c) and (d), The same but for  $a/b = 0.6$ .  $\Omega$  in the interior begins to decrease before being increased by the stressing rate from the accelerating right margin.

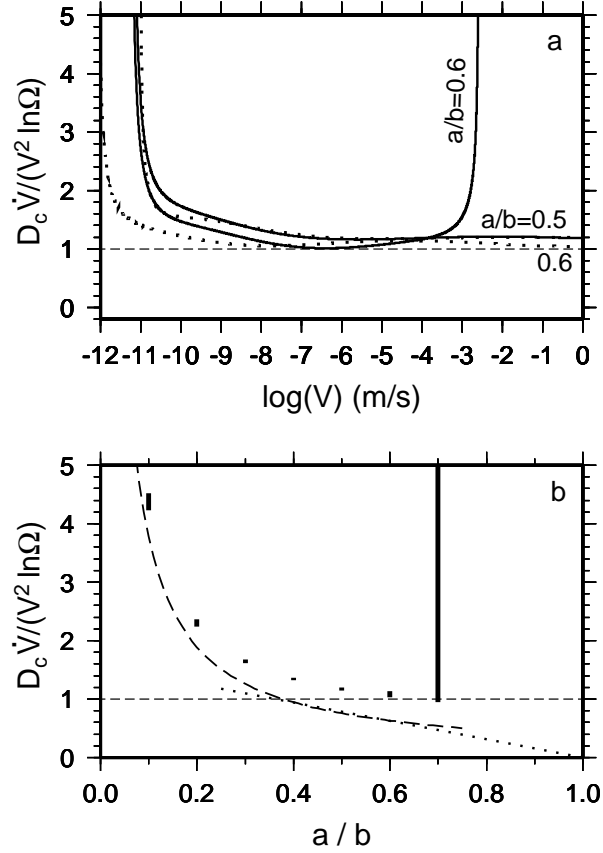


**Figure 6.** (a)  $D_c \dot{V} / (V^2 \ln \Omega)$  as a function slip speed, evaluated at the center of the nucleation zone, for  $a/b = 0.5$  and  $0.6$ . Solid curves are for the simulations in Figure 5; the curve for  $a/b = 0.6$  reaches a minimum of 1.01 before leaving the  $\Omega \gg 1$  regime. Dashed curves are for a locally peaked load on an otherwise uniform surface below steady state, subjected to a constant remote stressing rate. The curve for  $a/b = 0.6$  reaches a minimum of 1.04 and remains in the  $\Omega \gg 1$  regime. (b) Numerically-determined values of  $C' = D_c \dot{V} / (V^2 \ln \Omega)$  as a function of  $a/b$ , for 2 series of simulations with a locally peaked load on an otherwise uniform surface. The two simulations were designed to access a range of  $\Omega(V)$ . The vertical bars indicate the full range of  $C'$  for slip speeds  $10^{-3} < V < 10^4$  m/s. In general the difference between the two simulations is smaller than the variability within either, as with the  $a/b = 0.5$  examples in Figure 6a. For  $a/b = 0.7$  the simulations have left the  $\Omega \gg 1$  regime. For comparison, the dashed curve shows

$C_{\Omega \gg 1} = D_c \dot{V} / V^2 = 0.3781b/a$  for the aging law, expected to be applicable for  $a/b < 0.3781$ , while the dotted line shows  $C_{\Omega \sim 1} = (\pi/2)(1 - a/b)$ , applicable for larger  $a/b$ .

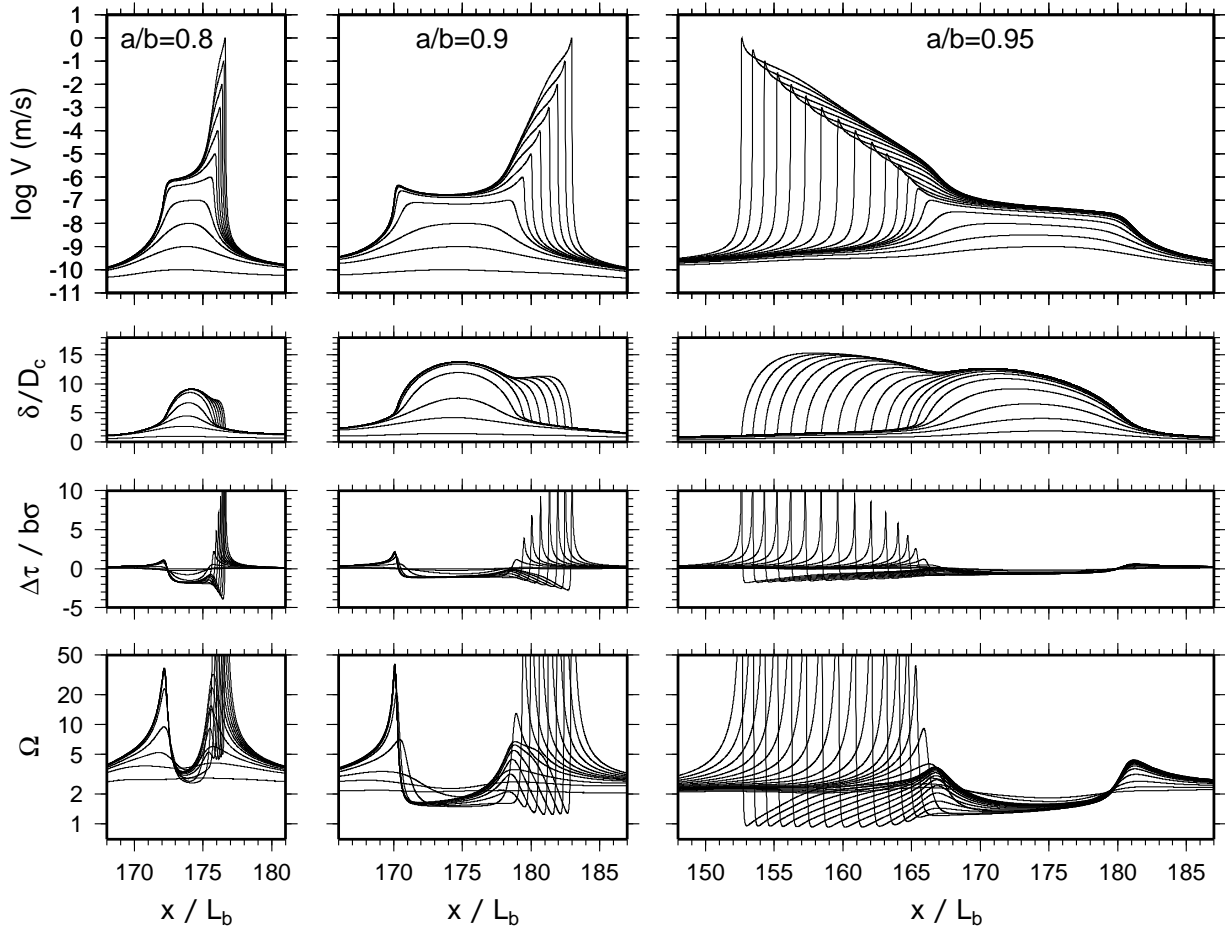


**Figure 7.** Snapshots from slip-law simulations with  $a/b = 0.8$  (left column), 0.9 (middle column), and 0.95 (right column). Initial and boundary conditions are as in Figures 3 and 5, but using a smaller grid spacing of 3 cm ( $\sim L_b/150$ ) to adequately resolve the nucleation front. Top row, slip velocity; second row, normalized slip accumulated since the first velocity snapshot; third row, normalized stress change; fourth row,  $V\theta/D_c$ .

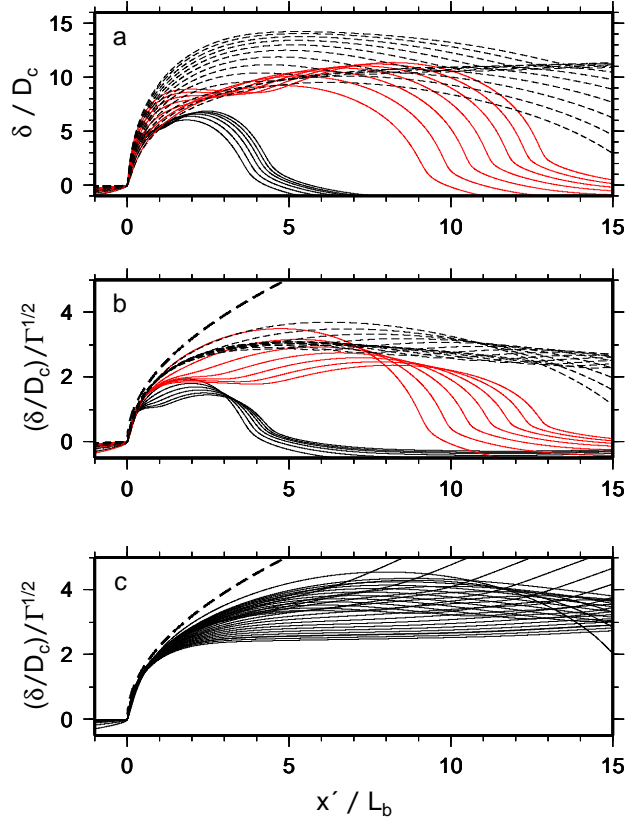


**Figure 8.** (a) Normalized slip as a function of distance behind the pulse tip for all snapshots in Figure 7 with  $V_{max} > 10^{-5}$  m/s (for  $a/b = 0.8$ ) and  $V_{max} \geq 10^{-6}$  m/s (for  $a/b = 0.9$  and  $0.95$ ). Slip has been offset to zero at the tip, and the horizontal axis has been reversed for  $a/b = 0.8$  and  $0.9$ . Dashed lines are for  $a/b = 0.95$ ; red lines for  $a/b = 0.9$ . (b) The same slip profiles further normalized by  $\Gamma^{1/2} \equiv [\ln(V_{max}\theta_i/D_c)]^{1/2}$ . The bold dashed line shows the estimate from equation (47). (c) The same as (b) but for the simulations of Figure 9 with  $V_{max} > 10^{-7}$  m/s.

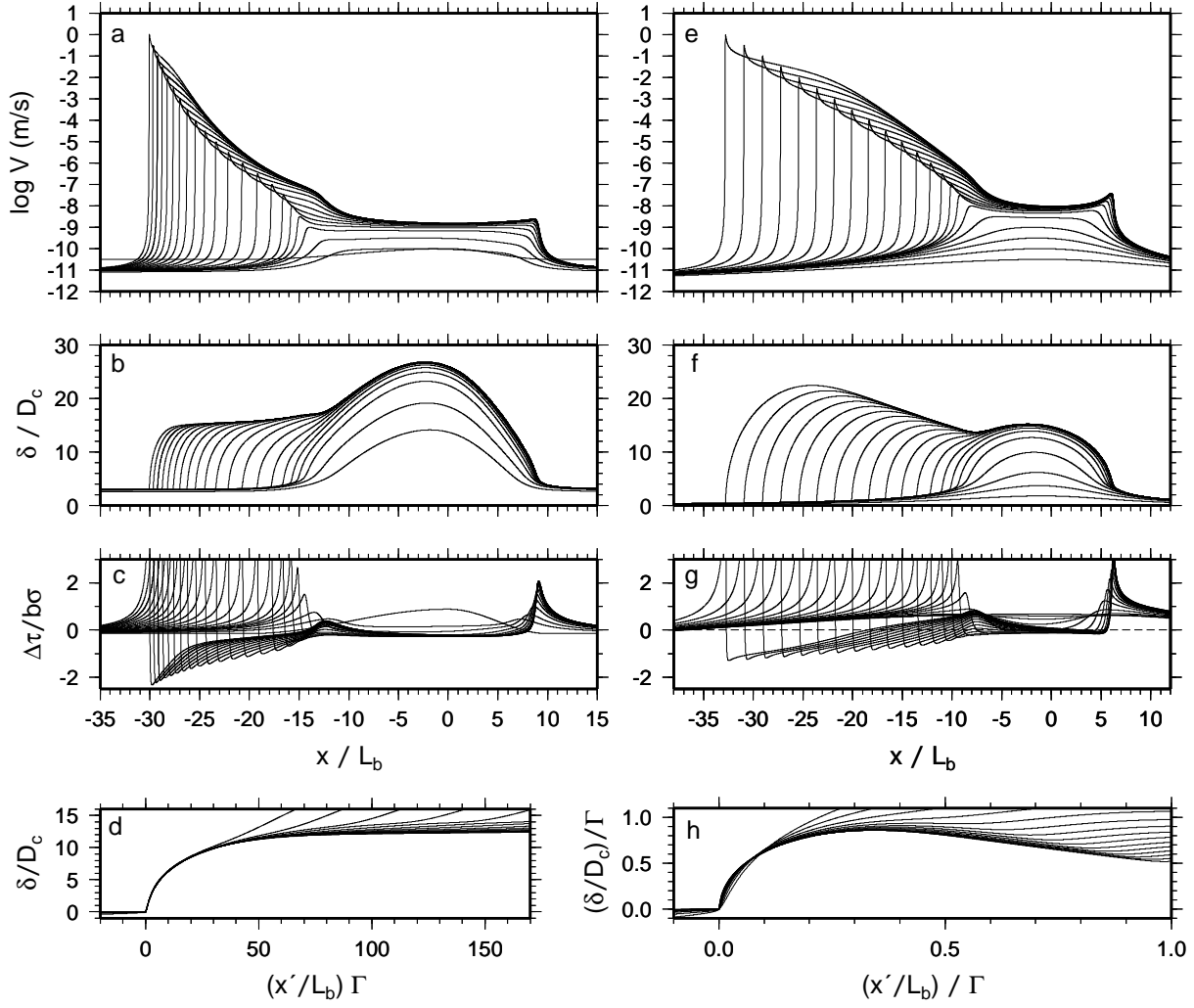


**Figure 9.** Snapshots of log slip speed (top row), normalized slip (second row), and normalized stress change from the local average (third row), for simulations with  $a/b = 0.9$  (left column) and 0.95 (right). The initial conditions consist of a uniform state and a locally peaked, slightly asymmetric velocity over a length scale of  $[b/(b-a)]L_b$ , such that the fastest gridpoint is slipping at steady state. In (d), the slip profiles corresponding to  $V_{max} \geq 10^{-7}$  m/s in (b) have been shifted so that the tip sits at (0,0) and the horizontal axis stretched by  $\Gamma \equiv \ln(V_{max}\theta_i/D_c)$  (equation 51). In (h), the slip profiles corresponding to  $V_{max} \geq 10^{-7}$  m/s in (e) have been normalized along both axes by  $\Gamma$ , and suggest an approach to self-similarity.

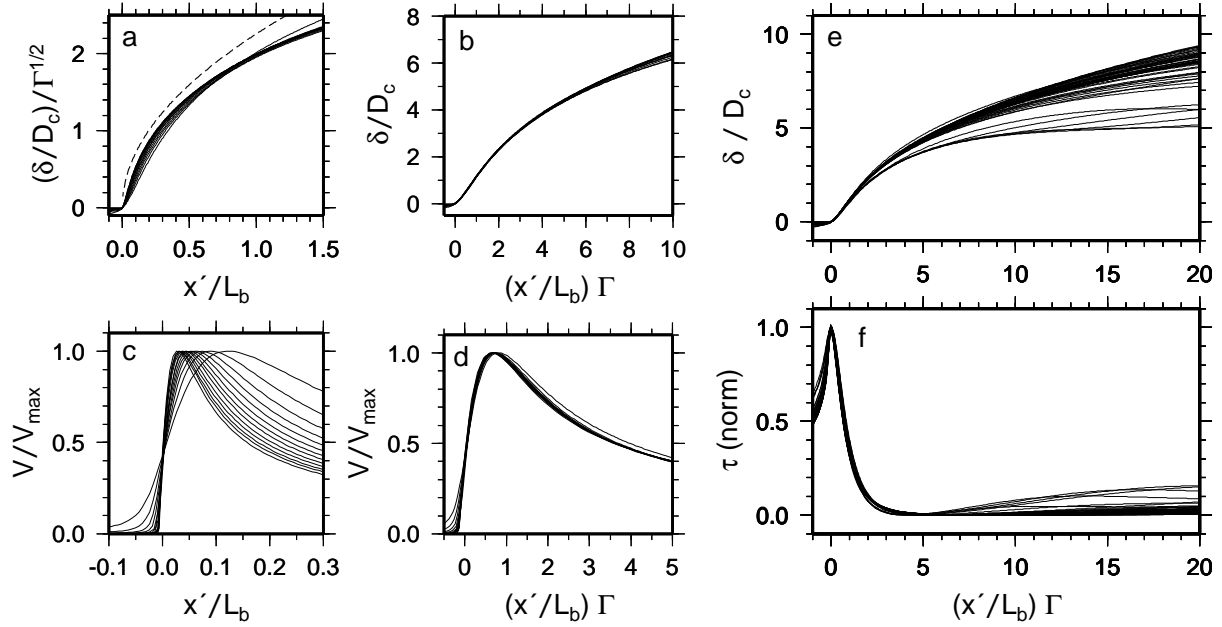


**Figure 10.** (a)-(d), Slip and velocity profiles for all the snapshots with  $a/b = 0.95$  and  $V_{max} \geq 10^{-6}$  m/s in Figure 7. (a), Normalized slip, scaled as suggested by equation (47), and (c), normalized slip speed, as functions of normalized distance behind the pulse tip. Dashed curve in (a) shows the expected value of  $(4/\pi^{1/2})(x'/L_b)^{1/2}$ . (b) and (d), Normalized slip and slip speed as functions of normalized distance from the tip, with the latter stretched by  $\Gamma \equiv \ln(V_{max}\theta_i/D_c)$  (equation 51). The collapsing of all the profiles from (a) and (c) shows that this is the appropriate scaling within the slip-weakening region. (e), Normalized slip as a function of scaled distance from the tip for all the slip profiles from Figures 8b and 8c, showing the universality of the near-tip slip profile. The cluster that deviates the most is for  $a/b = 0.8$  in Figure 7. (f), The stress profiles corresponding to the slip profiles of Figure 10e, scaled from a peak value of 1 to a minimum of zero.

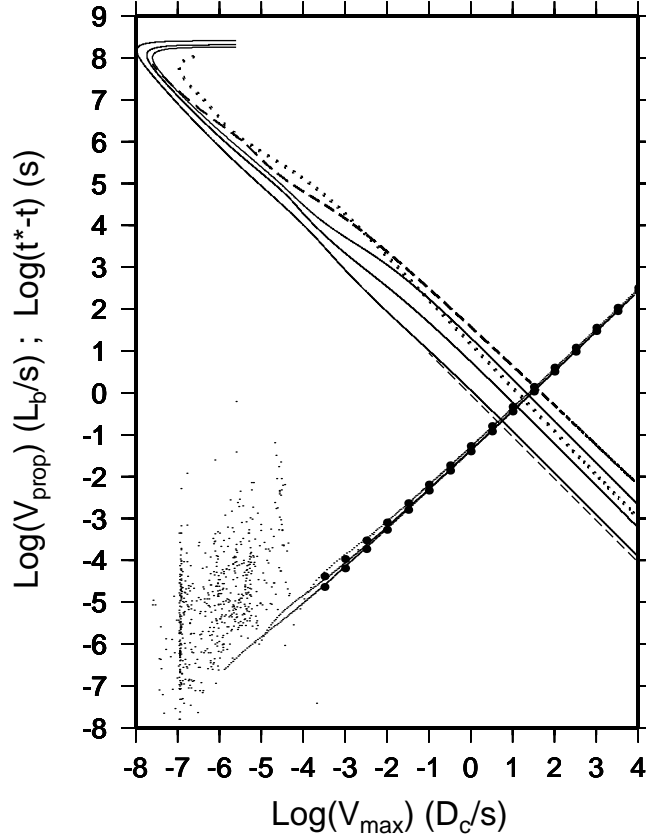


**Figure 11.**  $\text{Log } V_{prop}$  (ascending curves) and time to instability ( $t^* - t$ ) (descending curves) for the 5 simulations of Figures 7 and 9, as functions of  $\text{log } V_{max}$ . The scatter in  $V_{prop}$  at low slip speeds occurs before the nucleation zone is well developed. The two merging bold-dotted curves give the estimates of  $V_{prop}$  from (53) assuming values of  $\theta_i$  of  $10^6$  and  $10^8$  s, and show the insensitivity of  $V_{prop}/V_{max}$  to this parameter ( $\theta_i$  typically increases from a few times  $10^6$  to a few times  $10^7$  s over this range of  $V_{max}$ ). The 3 solid curves of ( $t^* - t$ ) correspond, from lowest to highest, to  $a/b = 0.8, 0.9,$  and  $0.95$  in Figure 7; these end with slopes of  $-1$  (lower dashed line), implying  $\dot{V}_{max}/V_{max}^2 = \text{constant}$ . The dotted and dashed curves of ( $t^* - t$ ) correspond to  $a/b = 0.9$  and  $0.95$  in Figure 9.

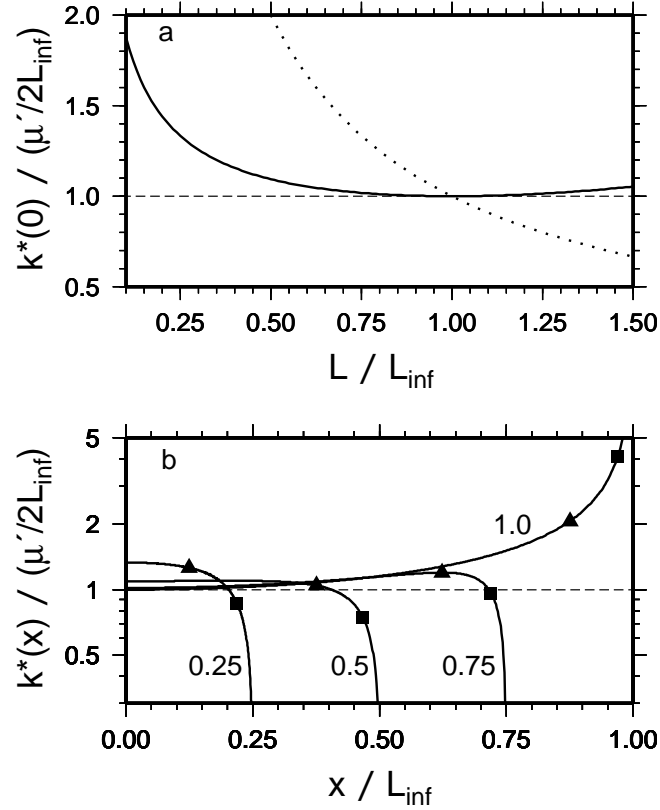


**Figure 12.** (a) Solid line, effective stiffness at the center of the growing nucleation zone,  $k^*(0)$ , normalized by the value for a crack of fixed half-length  $L_{\infty}$ , as a function of normalized nucleation length  $L/L_{\infty}$  (equation A5). The broad minimum near 1 shows that  $k^*(0)$  remains much closer to  $\mu'/2L_{\infty}$  than to  $\mu'/2L$  (dotted line). (b) Normalized stiffness as a function of position  $x/L_{\infty}$ , for  $L/L_{\infty} = 0.25, 0.5, 0.75$ , and 1.0, showing that  $k^*$  remains close to  $\mu'/2L_{\infty}$  over most of the growing nucleation zone as well (equation A7). Triangles and squares indicate a distance  $L_b$  behind the nucleation front for  $a/b = 0.8$  and 0.9, respectively; larger values of  $x$  lie near or within the slip weakening region where equation (A7) is inappropriate.

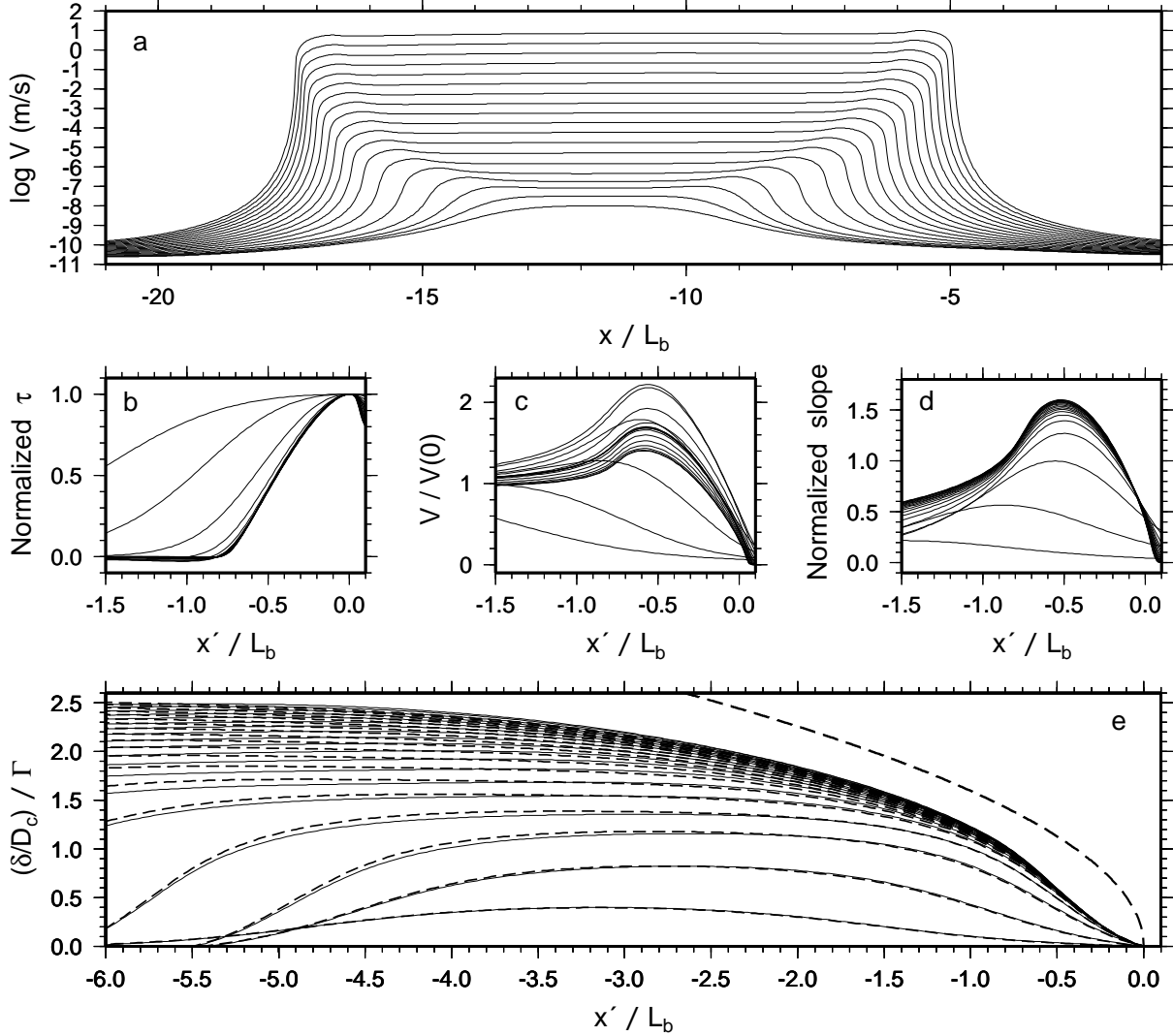


**Figure 13.** (a), Velocity profiles from Figure 3 with  $V_{max} \geq 10^{-8}$  m/s. (b), Shear stress, scaled from a peak value of 1 to zero at the center of the nucleation zone, as a function of normalized distance behind the right tip for all the profiles in (a). By the fourth profile the slip-weakening region asymptotically approaches  $\sim 0.75L_b$ . (c) Slip speed normalized by that at the center of the nucleation zone. (d) Normalized slip gradient  $(\delta/D_c)/(x'/L_b)$  for the same profiles, showing the maximum at  $\sim 0.5L_b$  that coincides with the peak slip velocity. (e) Normalized slip, divided by  $\Gamma \equiv \ln(V_{max}\theta_i/D_c)$  (equation B8), as a function of distance behind the right (solid) and left (dashed, and reversed for comparison) tips of the nucleation zone. Bold dashed curve indicates the prediction of (B10).

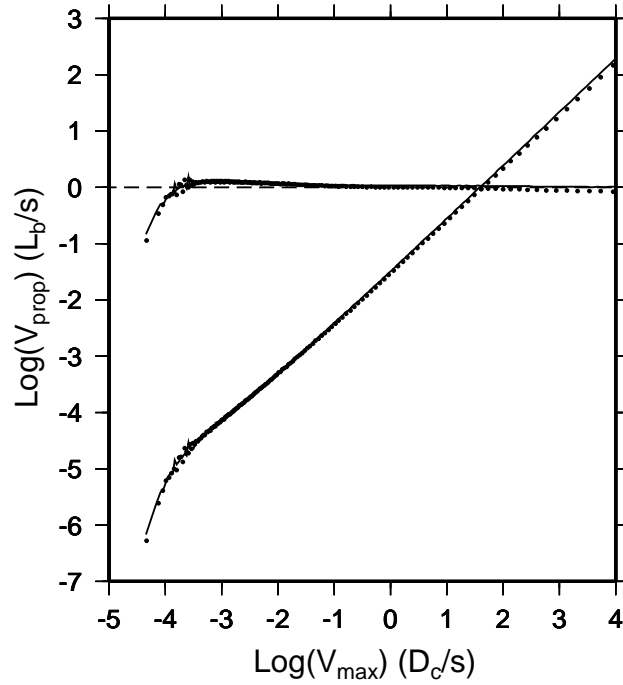


**Figure 14.** (Ascending curves)  $\text{Log } V_{prop}$  as a function of  $\text{log } V_{max}$  for the right (solid) and left (dotted) nucleation fronts in Figure 13. The factor of 2 difference in propagation velocities is explained by a comparable difference in  $V_{max}$ . (Horizontal curves) The numerical values of  $V_{prop}$  normalized by the prediction of (B10); dashed line indicates a ratio of 1. Equation (B10) is accurate to within a factor of 2 for  $V_{max} > 10^{-4} D_c/s = 4 \times 10^{-8} \text{ m/s}$ , i.e. by the second snapshot in Figure 13a.